AFRL-AFOSR-VA-TR-2017-0015

MULTIFUNCTIONAL THERMAL STRUCTURES USING CELLULAR CONTACT-AIDED COMPLIANT MECHANISMS

GEORGE LESIEUTRE
PENNSYLVANIA STATE UNIVERSITY
201 OLD MAIN
UNIVERSITY PARK, PA 16802-1505

01/26/2017
Final Report

Air Force Research Laboratory
AF Office Of Scientific Research (AFOSR)/RTB2

REPORT DOCUMENTATION PAGE

Form Approved
OMB No. 0704-0188

PLEASE DO NOT RETURN YOUR FORM TO THE ABOVE ORGANIZATION.

1. REPORT DATE *(DD-MM-YYYY)*	2. REPORT TYPE	3. DATES COVERED *(From - To)*
31-10-2016	Final Technical Report	Aug 2011 - Jul 2016

4. TITLE AND SUBTITLE
MULTIFUNCTIONAL THERMAL STRUCTURES USING CELLULAR CONTACT-AIDED COMPLIANT MECHANISMS

5a. CONTRACT NUMBER

5b. GRANT NUMBER
FA9550-11-1-0232

5c. PROGRAM ELEMENT NUMBER

6. AUTHOR(S)
Lesieutre, George, A
Frecker, Mary
Adair, James, H
Yu, Tianliang
Gigliotti, Christopher, M

5d. PROJECT NUMBER

5e. TASK NUMBER

5f. WORK UNIT NUMBER

7. PERFORMING ORGANIZATION NAME(S) AND ADDRESS(ES)
The Pennsylvania State University
Office of Sponsored Programs
110 Technology Center
University Park, PA 16802-7000

8. PERFORMING ORGANIZATION REPORT NUMBER

9. SPONSORING/MONITORING AGENCY NAME(S) AND ADDRESS(ES)
Air Force Office of Scientific Research
875 North Randolph Street
Arlington, VA 22203

10. SPONSOR/MONITOR'S ACRONYM(S)

11. SPONSOR/MONITOR'S REPORT NUMBER(S)

12. DISTRIBUTION/AVAILABILITY STATEMENT

DISTRIBUTION A: Distribution approved for public release.

13. SUPPLEMENTARY NOTES

14. ABSTRACT

Thermal management of spacecraft electronics is a major concern. Passive thermal control promises high reliability and reduced system weight. Cellular contact-aided compliant mechanisms were considered as an avenue to variable thermal conductivity. Thermally-driven deformation creates or breaks contact or modifies contact pressure, thereby controlling heat conduction through an interface. Pressure-dependent thermal contact conductance generates a smooth change between insulating and conducting modes. A topology optimization approach was conceived to maximize performance by placing two materials having very different conductivities. Several designs with good performance under realistic high and low heat loads were generated. Bi-material prototypes were fabricated from polished copper sheet. They achieved good conductance and rapid switching, especially those having low surface roughness. Future 3-D additive fabrication methods could conceivably produce the elegant but complex material and geometric designs contemplated. Continued research is needed to improve the robustness of the optimization scheme, as well as to fabricate and experimentally verify the thermal performance of the resulting designs in practice.

15. SUBJECT TERMS

spacecraft thermal management; passive thermal control; variable thermal conductivity; thermal contact conductance; topology optimization; cellular contact-aided compliant mechanisms

16. SECURITY CLASSIFICATION OF:			17. LIMITATION OF ABSTRACT	18. NUMBER OF PAGES	19a. NAME OF RESPONSIBLE PERSON
a. REPORT	b. ABSTRACT	c. THIS PAGE			George A. Lesieutre
U	U	U	UU	47	19b. TELEPHONE NUMBER *(Include area code)* (814) 863-0103

Reset

Standard Form 298 (Rev. 8/98)
Prescribed by ANSI Std. Z39.18
Adobe Professional 7.0

INSTRUCTIONS FOR COMPLETING SF 298

1. REPORT DATE. Full publication date, including day, month, if available. Must cite at least the year and be Year 2000 compliant, e.g. 30-06-1998; xx-06-1998; xx-xx-1998.

2. REPORT TYPE. State the type of report, such as final, technical, interim, memorandum, master's thesis, progress, quarterly, research, special, group study, etc.

3. DATES COVERED. Indicate the time during which the work was performed and the report was written, e.g., Jun 1997 - Jun 1998; 1-10 Jun 1996; May - Nov 1998; Nov 1998.

4. TITLE. Enter title and subtitle with volume number and part number, if applicable. On classified documents, enter the title classification in parentheses.

5a. CONTRACT NUMBER. Enter all contract numbers as they appear in the report, e.g. F33615-86-C-5169.

5b. GRANT NUMBER. Enter all grant numbers as they appear in the report, e.g. AFOSR-82-1234.

5c. PROGRAM ELEMENT NUMBER. Enter all program element numbers as they appear in the report, e.g. 61101A.

5d. PROJECT NUMBER. Enter all project numbers as they appear in the report, e.g. 1F665702D1257; ILIR.

5e. TASK NUMBER. Enter all task numbers as they appear in the report, e.g. 05; RF0330201; T4112.

5f. WORK UNIT NUMBER. Enter all work unit numbers as they appear in the report, e.g. 001; AFAPL30480105.

6. AUTHOR(S). Enter name(s) of person(s) responsible for writing the report, performing the research, or credited with the content of the report. The form of entry is the last name, first name, middle initial, and additional qualifiers separated by commas, e.g. Smith, Richard, J, Jr.

7. PERFORMING ORGANIZATION NAME(S) AND ADDRESS(ES). Self-explanatory.

8. PERFORMING ORGANIZATION REPORT NUMBER. Enter all unique alphanumeric report numbers assigned by the performing organization, e.g. BRL-1234; AFWL-TR-85-4017-Vol-21-PT-2.

9. SPONSORING/MONITORING AGENCY NAME(S) AND ADDRESS(ES). Enter the name and address of the organization(s) financially responsible for and monitoring the work.

10. SPONSOR/MONITOR'S ACRONYM(S). Enter, if available, e.g. BRL, ARDEC, NADC.

11. SPONSOR/MONITOR'S REPORT NUMBER(S). Enter report number as assigned by the sponsoring/ monitoring agency, if available, e.g. BRL-TR-829; -215.

12. DISTRIBUTION/AVAILABILITY STATEMENT. Use agency-mandated availability statements to indicate the public availability or distribution limitations of the report. If additional limitations/ restrictions or special markings are indicated, follow agency authorization procedures, e.g. RD/FRD, PROPIN, ITAR, etc. Include copyright information.

13. SUPPLEMENTARY NOTES. Enter information not included elsewhere such as: prepared in cooperation with; translation of; report supersedes; old edition number, etc.

14. ABSTRACT. A brief (approximately 200 words) factual summary of the most significant information.

15. SUBJECT TERMS. Key words or phrases identifying major concepts in the report.

16. SECURITY CLASSIFICATION. Enter security classification in accordance with security classification regulations, e.g. U, C, S, etc. If this form contains classified information, stamp classification level on the top and bottom of this page.

17. LIMITATION OF ABSTRACT. This block must be completed to assign a distribution limitation to the abstract. Enter UU (Unclassified Unlimited) or SAR (Same as Report). An entry in this block is necessary if the abstract is to be limited.

Final Report

AFOSR Agreement FA9550-11-1-0232

MULTIFUNCTIONAL THERMAL STRUCTURES USING CELLULAR CONTACT-AIDED COMPLIANT MECHANISMS

October 31, 2016

George A. Lesieutre
Mary Frecker
James H. Adair
Tianliang Yu
Christopher M. Gigliotti

Department of Aerospace Engineering
Department of Mechanical and Nuclear Engineering
Department of Materials Science and Engineering

The Pennsylvania State University
University Park, PA 16802

1. Background

Thermal management of electronic devices is a major concern in spacecraft; indeed, in all modern electronic systems [Hengeveld 2010]. Ineffective heat dissipation can lead to temperatures that exceed allowable hot or cold limits. And the reliability and predictability of passive systems make them the preferred choice over conventional active thermal control systems whenever possible. The basic aim of a passive thermal control system is to control heat transfer from electronic devices to a radiating exterior surface. Heat may need to be retained when the devices generate little heat, and high heat transfer efficiency is required when the devices generate excess heat.

Heat switches based on mechanical contact can be achieved in a variety of ways. Paraffin, because of the significant volume change when it melts, is used in heat switches. A gap between two devices is closed by melting paraffin when the device temperature approaches the high limit. Such heat switches have been used a number of applications, including the secondary batteries on the Mars Exploration Rover mission [Sunada *et al.*, 2002, Novak *et al.* 2003]. Differential thermal expansion (DTE) uses two materials with different coefficients of thermal expansion (CTEs) to control contact between the cold and hot sides of the switch. [Thomson *et al.* 2007], [Paulsen *et al.* 2000] and [Marland *et al.* 2000] built and tested a variety of DTE heat switches for cryogenic applications. [Milanez & Mantelli 2003] studied a bi-metallic heat switch for space applications theoretically and experimentally.

Contact-aided Cellular Compliant Mechanisms (C3M) are cellular structures with novel integrated contact mechanisms that provide local stress relief under high loads; when active, these contact mechanisms also introduce new thermal conduction pathways. Originally developed by Frecker and Lesieutre *et al.* [Mehta *et al.* 2008, Bharti *et al.* 2007, Lesieutre *et al.* 2006, Bharti *et al.* 2006, Ramrakhyani *et al.* 2005a, Ramrakhyani *et al.* 2005b] for potential application to morphing aircraft, C3M can be used in applications that would benefit from the capability to accommodate large strains. Under various thermal conditions, deformations of the structures create or break contact or modify the contact pressure, thereby effecting a thermal switch or "valve." This concept stands as a new approach for passive thermal control.

During this research effort, designs of increasing sophistication consistently outstripped the ability to fabricate them. Basic questions related to fabrication were addressed simultaneously with the thermal-structural design explorations.

2. Problem Overview

Electronic modules are a key component of Air Force satellites. These modules are designed to operate near room temperature (say 273 K – 293 K) and they can generate significant heat loads when operating. They are typically connected to the spacecraft bus structure via a thermal baseplate, as illustrated in Figure 1, and are intrinsically multifunctional. The thermal baseplate serves a structural function, in that it transfers mechanical loads, and a thermal function, in that it transfers heat away from (or insulates) the electronics modules in order to ensure that the electronics do not overheat (or become too cold).

In some cases, “thermal switches” are used for thermal control. Such switches operate to conduct heat when the electronics are working at the higher end of their design operating temperature range, and to insulate when the electronics are not generating a lot of heat. Both active and passive thermal switches are available, but the passive ones are preferred for reduced power and control complexity. Some passive thermal switches are available, based on paraffin blends, for example, but these perform better at temperatures that are colder than desired. There is a real need for variable thermal conductivity materials that can change passively from low to high conductivity around room temperature, while also carrying nominal structural loads.

An ideal variable thermal conductivity structure would have conductivity (k) comparable to that of aluminum (247 W/(m·K)) on the high end and, on the low end, at least an order of magnitude lower. (Zirconia, a ceramic of potential interest for fabrication, has a thermal conductivity on the order of 2 W/(m·K).) The higher the switching ratio (k_{high} / k_{low}), the less makeup heat must be provided to keep the electronics warm when the thermal switch is in its low-conducting state. Eliminating the need for makeup heat would significantly reduce the weight of the thermal control system, as supplemental batteries, heaters, and control become unnecessary.

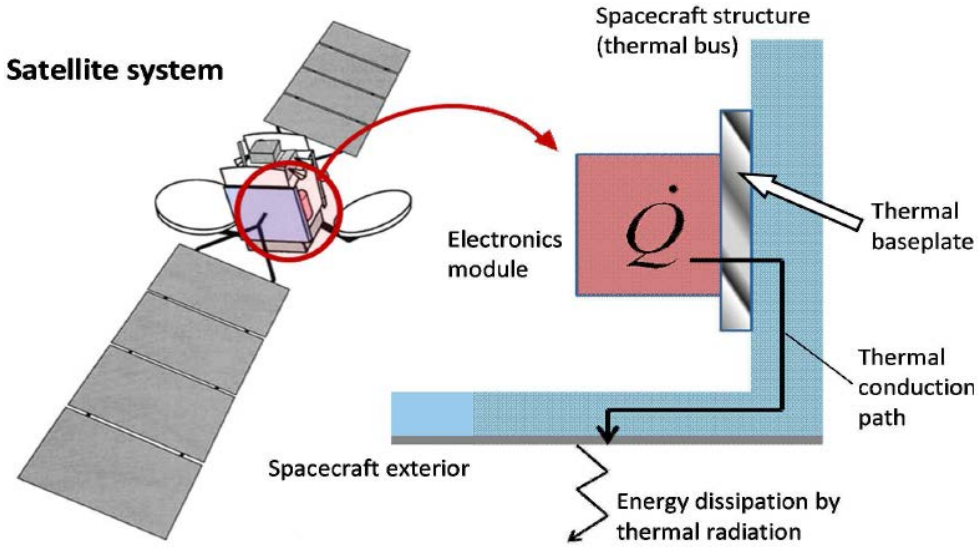

Figure 1. Typical heat conduction path from the electronics module to the thermal bus until dissipation

The overarching goal of the research in this report is the development of a variable thermal conductivity structure suitable for application to spacecraft thermal control. One potential concept of operation is as follows:

1. When the “hot side” of the thermal baseplate is below some threshold temperature, the baseplate is in a thermally-insulating state, associated mainly with the ceramic part of the C3M. The C3M structure carries nominal mechanical mounting loads as well.
2. The CTE of the ceramic-metal C3M structure is designed so that as the temperature of the “hot side” increases above some threshold value, the structure expands and internal contact is made between conducting members, increasing the thermal conductivity of the baseplate—dramatically or gradually, depending on the interface. This conductivity is maintained at higher temperatures.

3. As the baseplate heat load is reduced and its temperature falls, thermal contraction of the C3M causes the conductive contact to weaken then break, returning the baseplate to an insulating state. If the conductivity is small enough, the base electronics heat load is adequate to maintain its temperature at an acceptable point.

Figure 2 shows a potential concept of operation of a C3M device in which the deformation driven by the temperature distribution and DTE creates or closes the contact gap.

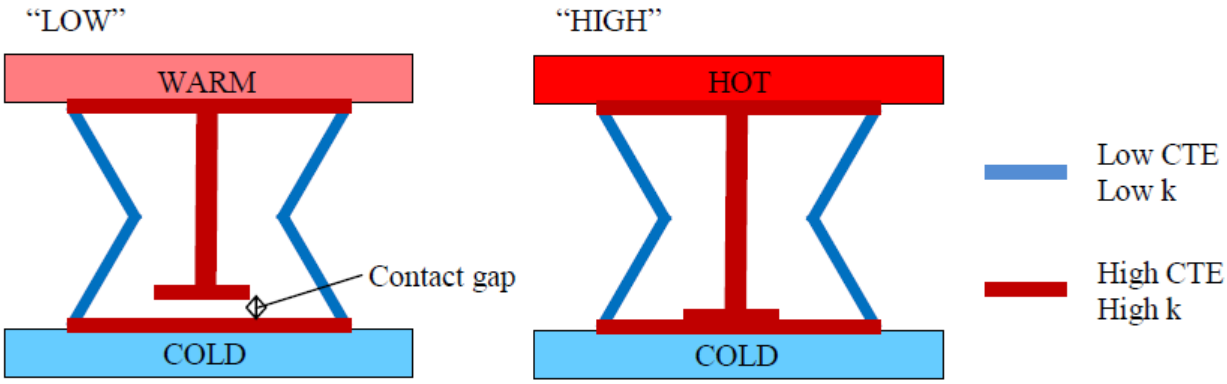

Figure 2. A thermal switch concept based on the deformation of C3M device

3. Design and Fabrication Approaches

This section briefly describes three design approaches that were pursued to achieve the research goals, as well as several fabrication approach that were pursued to realize one of the designs.

3.1 T-shaped contact-aided cells

In early research, a structural thermal switch that uses a compliant structural cell with an internal contact interface was characterized using a finite element method and subjected to thermal loads typical for spacecraft equipment. The *thermal contact resistance* (TCR) as a function of pressure was adopted to model thermal conduction between the two sides of the contact interface. TCR depends greatly on the pressure at the interface, which makes the structure less of a discrete step-change "switch" between modes and more like a continuous thermal "valve." A 2D T-shaped cell consisting of two materials with different CTEs was modeled in ANSYS. Parametric studies of different boundary loading combinations were conducted to find optimal geometries.

3.2 Fabrication of T-shaped contact-aided cells

During the initial phases of the project, the lost-mold rapid infiltration manufacturing (LM-RIF) process developed at Penn State was evaluated as a microfabrication strategy [Antolino, Hayes *et al.*, 2008; Hayes 2011]. It was used to prepare the thermal conduction and heat sink material, with 316L stainless chosen initially because of the availability of well-defined spherical particles. However, the LM-RIF process proved to be unreliable in processing the relatively large 316L particulates with low edge resolution because of large grains (~100 microns grain size) and steel debris in the contact area, shown in Figure 3. Furthermore, evaluation of the stress-strain behavior for the tensile specimen indicated an unreliable sintered material with a wide range of mechanical property behavior for the materials.

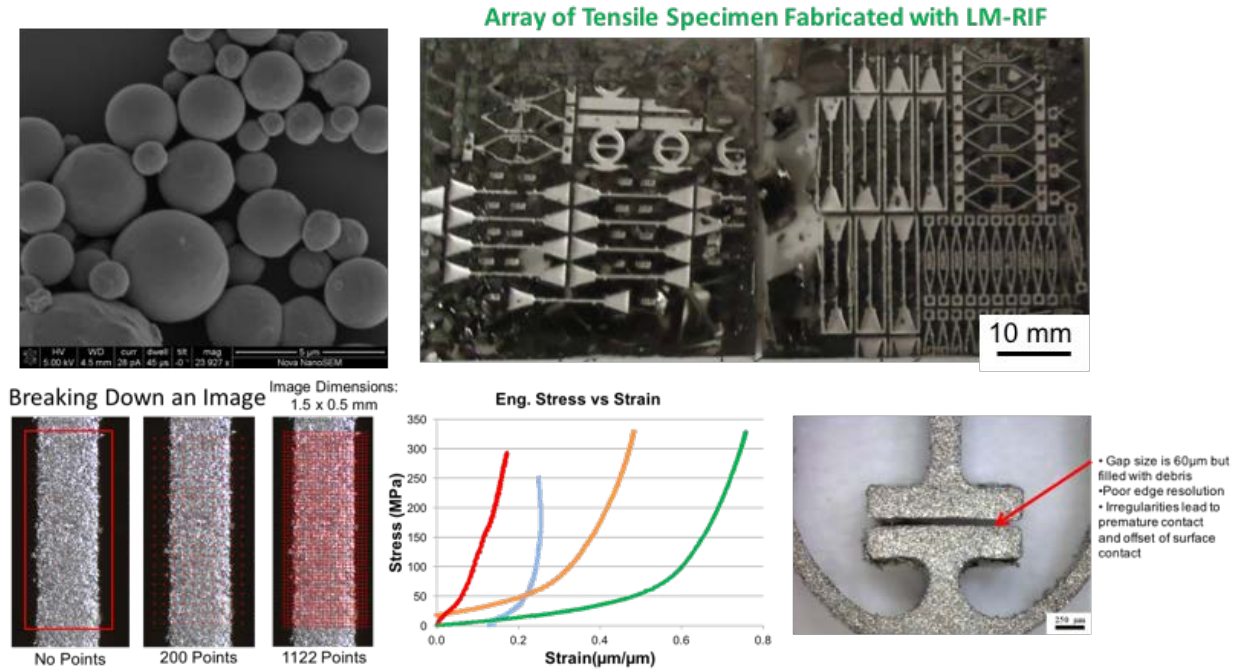

Figure 3. 316L SS particles, tensile specimen, and a contact gap made using the LM-RIF process

The LM-RIF experimental fabrication efforts showed that the high resolution contact gap (~10 microns) was not yet attainable using the metal powders currently available. Therefore, a modified strategy was evaluated in which copper nanoparticle synthesis was evaluated (Figure 4). The Cu nanoparticles dispersed efficiently with a polyvinylpyrrolidone dispersant, but the ~500 nm diameter particles were composed of agglomerated masses of even finer nanoparticles that compromised the high packing density required for the LM-RIF process.

The T-shaped contact-aided cell was fabricated using an alternative method based on commercially available sheet materials and mechanical polishing of the metal surfaces at the gap. Copper, with a thermal conductivity (k) of 401 W/m-K and a coefficient of thermal expansion (CTE) of 16.6 ppm/K and alpha-alumina (α-Al_2O_3), with k at 30 W/m-K and CTE at 8.1 ppm/K were selected for the high thermal conductivity and low thermal conductivity materials in the fabricated component, respectively.

3.3 Topology optimization using non-dimensional models

In continuing design research, a topology optimization approach was crafted to maximize the thermal performance of the structure. Based on a finite element formulation and Solid Isotropic Material with Penalization (SIMP) interpolation for material properties, topology optimization was used to determine the distribution of multiple materials in C3M cells. The Method of Moving Asymptotes (MMA) was used as the scheme for seeking specific values of the design variables. The objective function was the global mechanical / thermal compliance of the structure. A thermal contact model based on unilateral contact used a Newton's method to solve the governing equation with nonlinear boundary conditions. Rather than aiming to design structures with complete detail, the model is intended to highlight possible features that could be

included in future C3M designs, hence non-dimensional parameters (not actual physical values) were used.

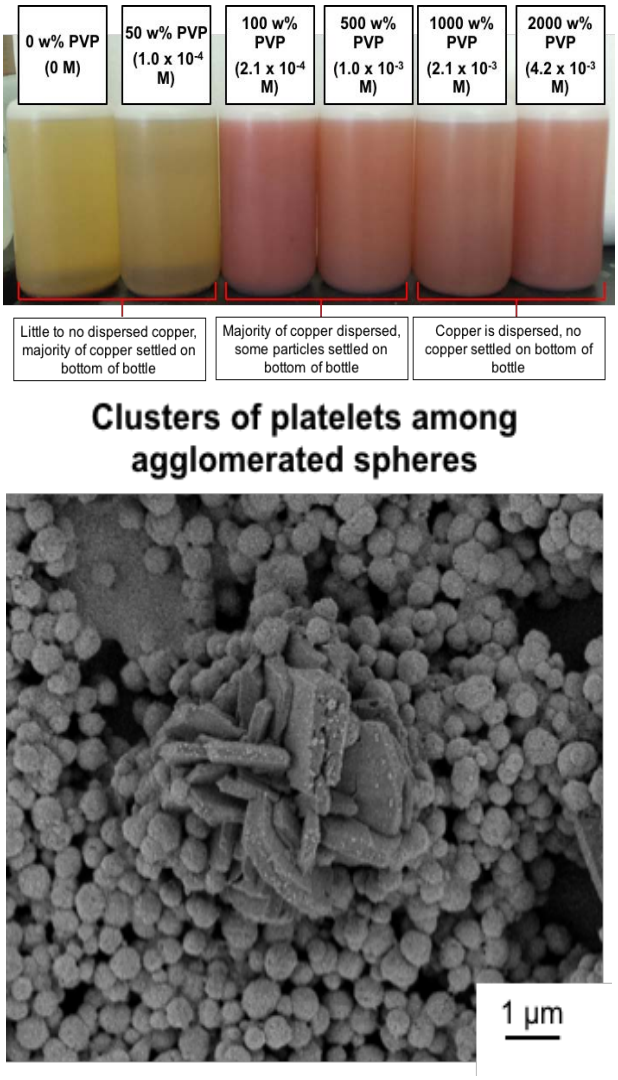

Figure 4. (top) Copper nanoparticle dispersion and (bottom) photomicrograph of 500 w/o PVP sample

3.4 Topology optimization using real dimensional models

Based on results uncovered during the preceding approach, and to simplify the physics, an "always-contact" model was proposed such that the entire potential contact surface is assumed to always be in contact with the heat sink. The variance of the effective thermal conductivity (TCR) then only depends on the contact pressure, which is itself determined by the thermal load condition. A one-dimensional analytical solution verified the feasibility and numerical efficiency of this simplification. A 2-D topology optimization approach using rectangular finite elements was then used to develop a design approach for rectangular C3M cells, using model parameters representative of typical spacecraft thermal control situations. Even with these simplification, nonlinearity is still present in the governing equations. A novel method of iteratively determining the temperatures at the bottom surface nodes was used to address the nonlinear coupled

governing equation. And with the objective function defined in a more straightforward way, the average temperature of the top surface of the cell can be readily established.

4. Results and Discussion

This section summarizes the major results obtained using the methods described.

4.1 T-shaped contact-aided cells

The considered T-shaped contact-aided cell is shown in Figure 5(a). The dark color column in the center of the cell is made of low-CTE and low-thermal-conductivity material, while the brighter parts are made of high-CTE and high-thermal-conductivity material. When the heat flux is relatively low, thermal expansion of the device is not large enough to close the gap, so the heat flows through a long, low-conductivity path (having high- and low-conductivity materials in series) to provide effective insulation, as shown in Fig. 5(b). When the temperature change is sufficiently large, the structure expands to close the gap with some pressure. The heat then flows more directly to the contact area through a high-conductivity path, as shown in Fig. 5(c).

4.1.1 Model for thermal contact resistance (TCR)

One of the major variable aspects of the T-shaped contact-aided cells is the thermal resistance between the interfaces at the contact region, also known as the thermal contact resistance (TCR). TCR is defined consistent with Fourier's law of heat conduction, in which the heat flux is proportional to a temperature gradient:

$$TCR = \frac{\Delta T_{interface}}{q} \tag{1}$$

where q is the heat flux through the contact surface, and $\Delta T_{interface}$ is the temperature difference across the contact interface, as shown in Figure 6.

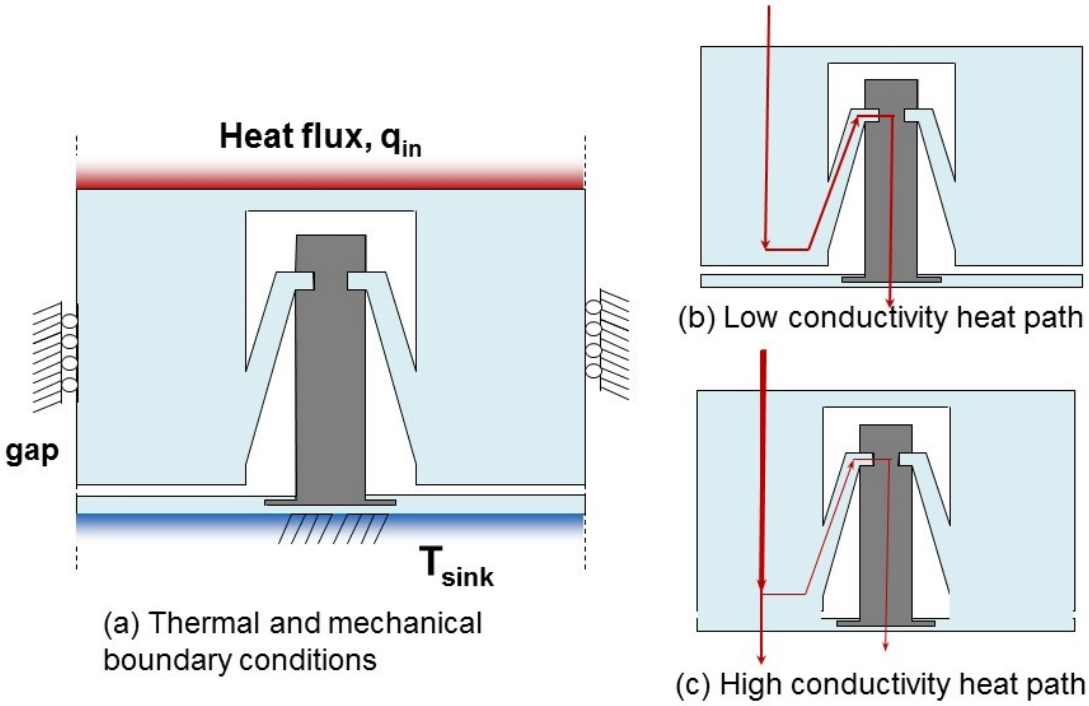

Figure 5. Design of the T-shaped cell

In this research, the TCR model developed by Antotelli *et al.* [Antotelli *et al.* 2003], based on empirical data for metal-to-metal contact, was used to characterize the cells. This model gives a general relation for thermal contact conductance (the reciprocal of TCR) as shown below:

$$\frac{1}{TCR} = h_c = 4200 k_s R_a^{-0.257} \left(\frac{P}{H}\right)^{\beta} \tag{2}$$

where k_s is the harmonic mean of the thermal conductivity of the two material in contact [W/(m·K)]; R_a is the average surface roughness (μm); P is the normal pressure (Pa); H is the surface micro-hardness (Pa); and β is a coefficient between 0 and 1, usually taken to be 0.95.

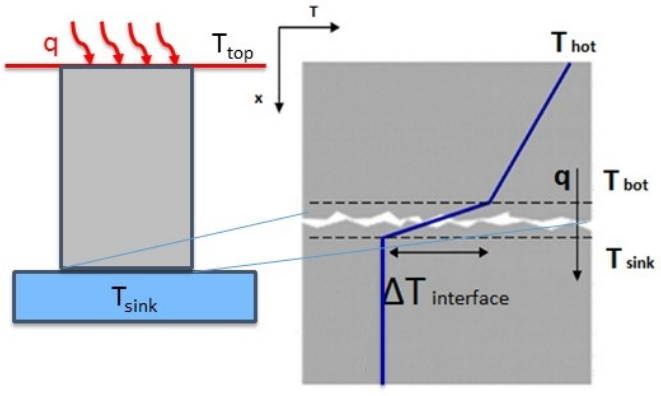

Figure 6. Temperature difference across the contact interface

This model was chosen for use in this research because it has been shown to be fairly reliable for metal interfaces and it is an analytical expression that is relatively easy to incorporate into a larger engineering model. It has the additional benefit that it only relies on the average roughness of the surface and does not include asperity slope as do other popular models. Finally, most of the model parameters are fixed by material selection and surface finish, and the only remaining variable is contact pressure. The equation can thus be generalized as:

$$\frac{1}{TCR(p)} = h_c(p) = TCC_0 P^{\beta} \tag{3}$$

4.1.2 Parametric study

The proposed unit cell and the variables that define its geometry are shown in Figure 7. Table 1 shows the material properties and the ranges of geometric parameters ranges used in the parametric study. Other variables include T_{ref}, T_{sink}, q_{in}, TCC_0 and β. The shape is studied using FEM under quasi-static (steady-state) thermal response in ANSYS. The out-of-plane geometry is taken to be unit-depth for all elements, and plane stress is assumed. All displacements are in-plane only. Observations from the parametric study are discussed in the next section. Further details, results and discussion can be found in [Stavely 2013].

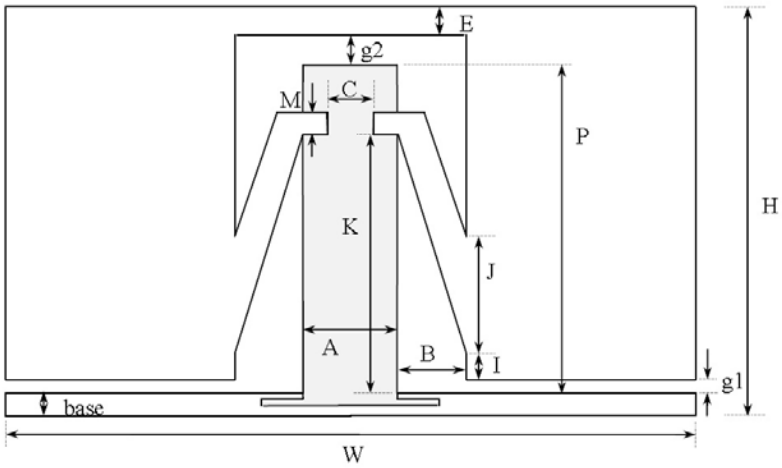

Figure 7. Geometry of the T-shaped cell

Table 1. Material and geometric parameters ranges for the T-shape cell

Geometry

Direct Inputs		Factors		Geometry Relations
*g1	0.00	a	0.01 - 0.9	A = a*D
g2	100 μm	b	0.01 - 0.9	B = b*D
W	0.01 m	c	0.01-0.9	C = c*A
E	0.0005 m	k	0.01 - 0.9	K = k*P
H	0.0025 - 0.01m	m	0.01 - 0.9	M = m*P
*g1 = Contact gap at reference temperature		i	0.01 - 0.9	I = i*H
		j	0.01 - 0.9	J = j*H
				P = H-E-g2

Materials

Material Model	**Thermal Conductivity, k [W/mK]**	**CTE, α [μm/mK]**	**Modulus of Elasticity, E [GPa]**	**Poisson Ratio, ν**	**Yield Tensile Stress, σ_{yield} [MPa]**
Material 1	350	16	100	0.3	200
Material2	10	10	200	0.3	200

4.1.3 Observations to guide future designs

Guidance for future designs were gleaned from the parametric study as follows:

- In a taller cell, the importance of bulk resistance tends to be larger than that of the contact resistance. The overall response is less sensitive to TCR than that of a shorter cell.
- The reference temperature should be set lower than the switch temperature, in order to achieve a better switch to the low-conductivity mode.
- If TCC_0 and β can be relatively high, then the optimal stress-limited design is a short cell with a reference temperature close to the switch temperature. In order to get higher effective conductivity values as TCC_0 and β are decreased, the cell height must be increased and the reference temperature decreased further below the switch temperature.
- The contact area has a greater effect on effective conductivity than contact pressure.

4.2 Fabrication and characterization of T-shaped contact-aided cells

The possibility that a high conductivity structure (in series with a low thermal conductivity substrate) would, upon expansion, thermally associate with a lower high thermal conductivity metal structure was investigated experimentally (Figure 8). As noted previously, copper and alpha-alumina (α -Al_2O_3) were used as the high thermal conductivity and low thermal conductivity materials in the fabricated component, respectively. Both are commercially available in sheet prototype form. The as-received sheets (nominally 0.5mm) were cut via waterjet and diamond cutoff wheel into the configurations specified. The thermal conduction module and heat sink each measured 2.54 cm by 1.27 cm.

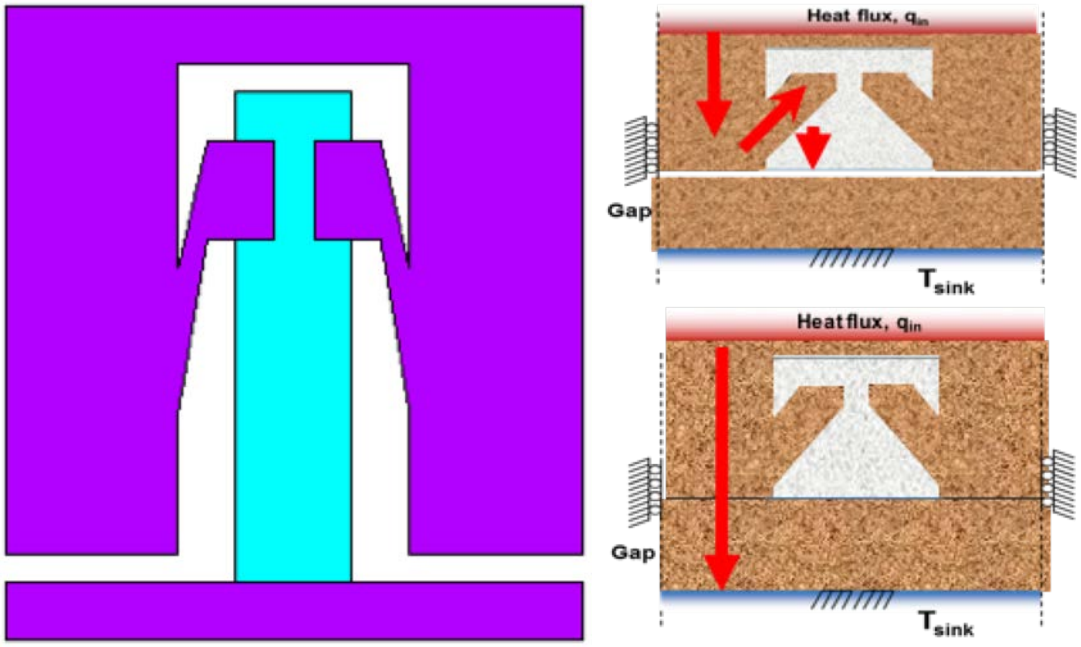

Figure 8. (left) design from (Stavely 2013); (right) fabricated thermal switch, 'open' and 'closed'

4.2.1 Polishing

The copper parts were mounted in acrylate to enable automated polishing of the interface between the thermal conduction module and heat sink, using 200 micron yttria-stabilized-zirconia milling media at the polishing surface. [Adair *et al.*, 2016] An unpolished group and 3 treatment groups were compared (n=3 for each set of samples). Nine samples were polished for 1 hour using 800 (P-2400) grit silicon carbide paper with 150 rpm plate speed, 150 rpm sample rotation, and 6 lbf. Six samples were polished for an additional hour, and three of these samples then received an additional polishing step with white label polishing cloth and greenlube at 4 lbf for two 2-minute cycles. All the samples were then submerged in an acetone bath for two weeks to remove excess acrylate.

4.2.2 De-oxidation

After mechanical polishing, the copper parts were subjected to a surface de-oxidation process. The copper parts were placed into a solution containing 10 grams of NaCl in 60 mL dilute acetic acid for 10 seconds before being rinsed with deionized water.

Thermal emissivities were found to be 0.04 and 0.84, for polished copper and copper with a copper oxide surface, respectively. For the $8cm^2$ surface area of the fabricated design, the relative radiant conductance (compared to the thermal conductance) was insignificant at $<1x10^{-7}$ for both polished and oxidized copper. The copper sheet was polished for various lengths of time to evaluate thermal conductance with different surface roughnesses.

4.2.3 Characterization

Prior to assembly, gap interfaces were analyzed to determine surface roughness. Optical micrographs of the gap interface edge were taken using an inverted optical microscope, and FE-SEM was performed to provide a more accurate representation. Each sample was also measured using a 3D Optical Profilometer with a 10X objective at 0.5X zoom that had enough resolution to view the surface roughness and the edges of the sample while allowing the width of the sample to be measured in a single scan. Optical profilometry data was analyzed to determine Sa (arithmetic mean of the surface roughness), Sq (geometric mean of the surface roughness, and Sz (range between maximum and minimum) data.

4.2.4 Assembly

The upper conduction module was glued using a 2-part epoxy to the α-Al2O3 substrate, which in turn was glued to a larger α-Al_2O_3 substrate. The lower thermal heat sink was bonded to the lower α-Al_2O_3 substrate with an alumina spacer to ensure that the two metal surfaces were aligned upon thermal expansion. The interface between the thermal conduction module and the heat sink were placed into zero-pressure contact before the epoxy hardened.

4.2.5 Thermal Characterization

Four thermocouples were attached to the copper face of an assembled T-shaped cell using Kapton tape. The cell was then sandwiched between two 2-inch square slabs of copper, one providing the heat source via a flexible heater rated at 5 W/in^2 (0.78 W/cm^2) and the other acting as a heat sink (Fig. 9a). To ensure contact between the heat source, prototype, and heat sink, Kapton tape was used to secure all parts in place. Electrodes were also placed to measure gap electrical resistance. Optical micrographs of the gap were also taken at various times (Fig. 9b).

Power was supplied to the heater and the system was allowed to reach a steady state temperature (t=50 min). During this time, temperatures at the 4 thermocouple locations were collected, electrical resistance across the interface was measured continuously, and optical micrographs were taken at t=0, 15, and 50 minutes (Figure 10). Steady state conditions were used to determine conductance for each of three fabricated switches as a function of surface roughness in the contact area. The measured values were compared to theoretical values as a function of the calculated contact pressure. This experimental procedure was repeated three times for one representative sample from each of the four polishing treatment groups.

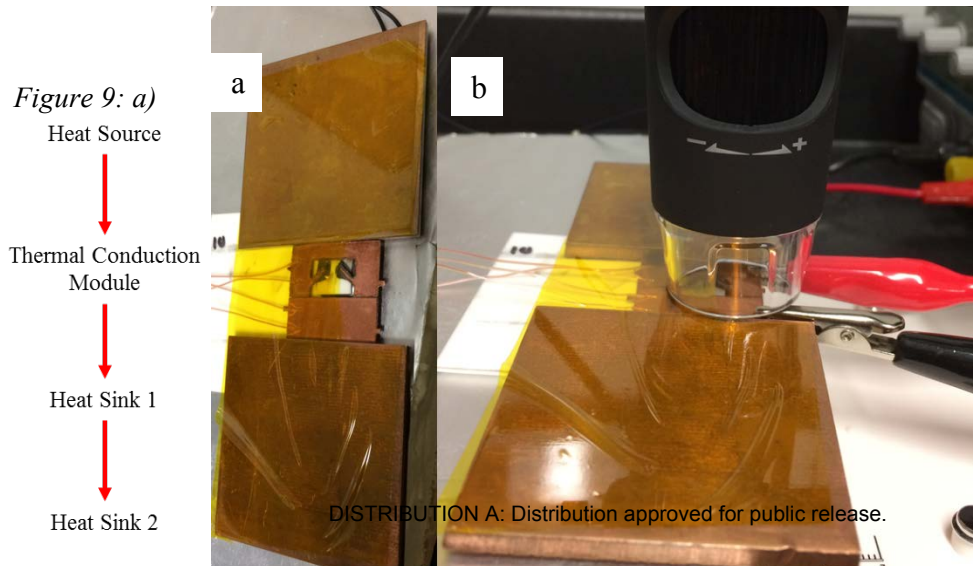

Experimental orientation. b) Data collection setup

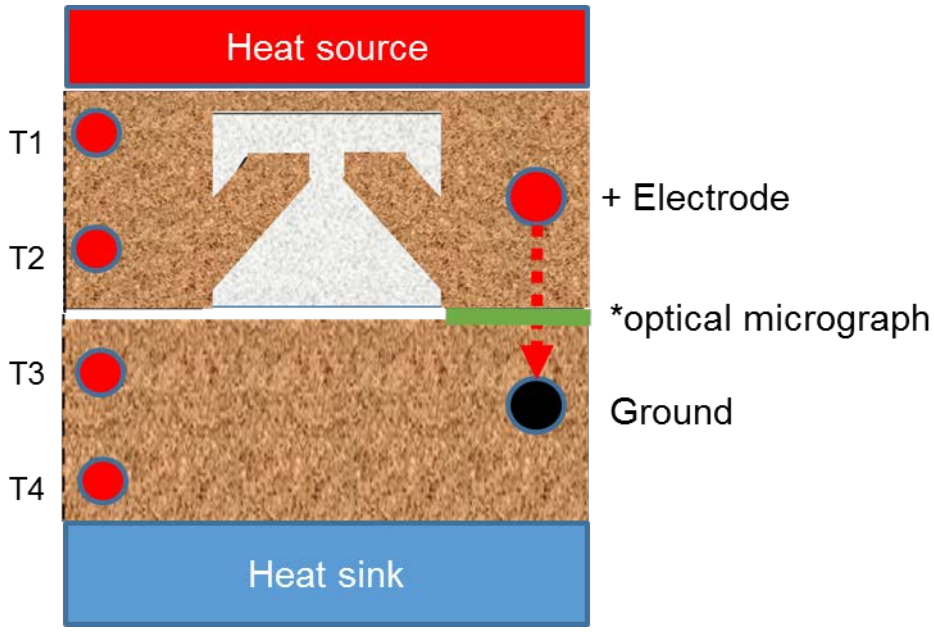

Figure 10. Data Collection Schematic for (Left side) temperature (T1 through T4 with T2 and T3 temperatures used to determine thermal contact conductance) and (Right side) electrical resistance

4.2.6 Surface Roughness vs. Polishing

The resulting range of interface surface roughness for the copper parts (Ra is shown in Figure 11) provided a range of values to be tested against design models. Fabrication of thermal switches proceeded with four of the polished copper parts, with three devices made for each polishing time. The surfaces of four selected samples were examined via optical profilometry (Figure 12), Optical microscopy (Figure 13), and FE-SEM (Figure 14). Each of the imaging modes underscores the effect of the mechanical polishing on surface roughness. The as-received water jet cut copper samples (CMG4-1-6) has a tortuous surface with an Ra = 27.6 ± 3.9 μm in contrast to CMG4-1-21, that, after 2 hours of polishing followed by lapping has an Ra = 1.6 ± 0.5 μm with a dramatically different surface indicated in images in Figures 12, 13, and 14. While surface roughness does not overwhelming affect thermal contact conductance, the switching time evaluated using electrical resistance measurements across the gap as a function of time and temperature indicates a dramatic difference due to surface roughness.

4.2.7 Switching time via electrical resistance

The only sample without a large switching time was CMG4-1-21 with Ra = 1.6 ± 0.5 μm (Figure 15). The gap was small at the onset and became smaller with increasing time and temperature, the temperature estimated to be about 24 C at the electrode on the heat sink as opposed to the temperature at T2 of about 28 C in Figure 16 (bottom). The time required to achieve baseline resistance was 60 s. In contrast, the other three samples had poor correlation of thermal response with electrical resistance. The as-polished sample, CMG4-1-6, with the highest roughness and with a ridge at the edge of the sample did not have a detectable change in electrical resistance with increasing temperature. The two intermediate Ra samples, CMG4-1-10 and CMG4-17, gave an initial drop to a plateau in time and temperature that resulted in switching times greater than 5

minutes. A higher contact pressure (and by association, temperature) would be required to achieve the same TCC as a contact zone with a smaller surface roughness. Thus, surface roughness not only plays a role in TCC, but also in switching time.

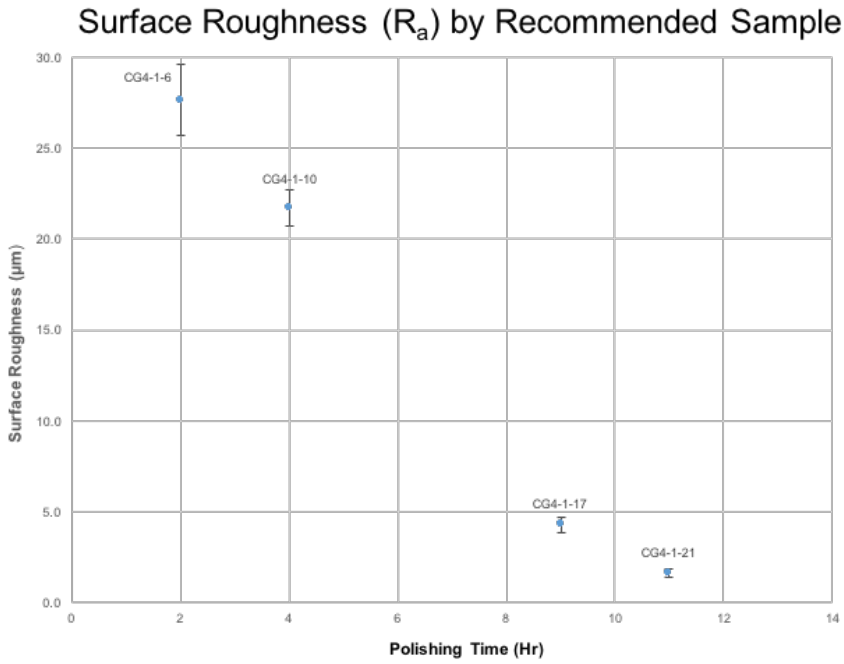

Sample	R_a (µm)	Conf. Int.
CMG4-1-5	20.6	3.29
CMG4-1-6	27.6	3.87
CMG4-1-7	14.6	3.73
CMG4-1-10	21.7	1.98
CMG4-1-11	21.3	6.15
CMG4-1-12	16.60	3.09
CMG4-1-15	9.8	11.98
CMG4-1-16	13.50	16.71
CMG4-1-17	4.31	0.82
CMG4-1-20	3.23	1.04
CMG4-1-21	1.64	0.52
CMG4-1-22	5.82	3.32

Figure 11. Polished copper thermal conduction and heat sink module surface roughness. Highlighted samples were used to fabricate thermal switches.

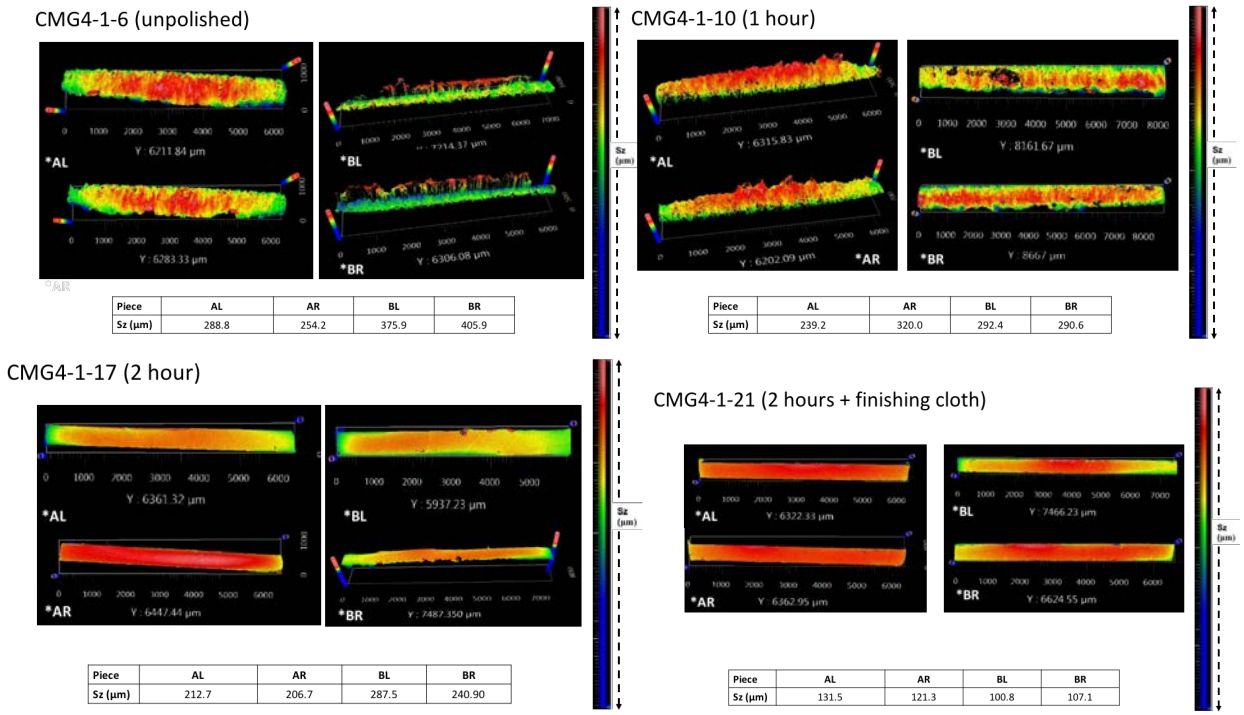

Figure 12. Representative optical profilometry images for each of the four selected copper specimens

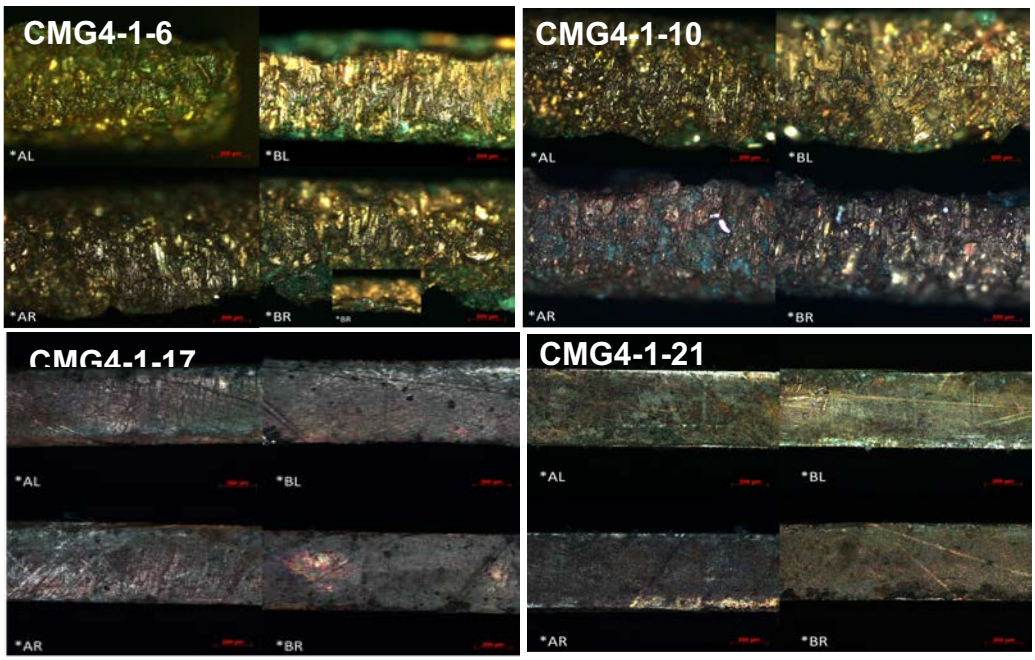

Figure 13. Representative optical photomicrographs of each of the polished copper specimen

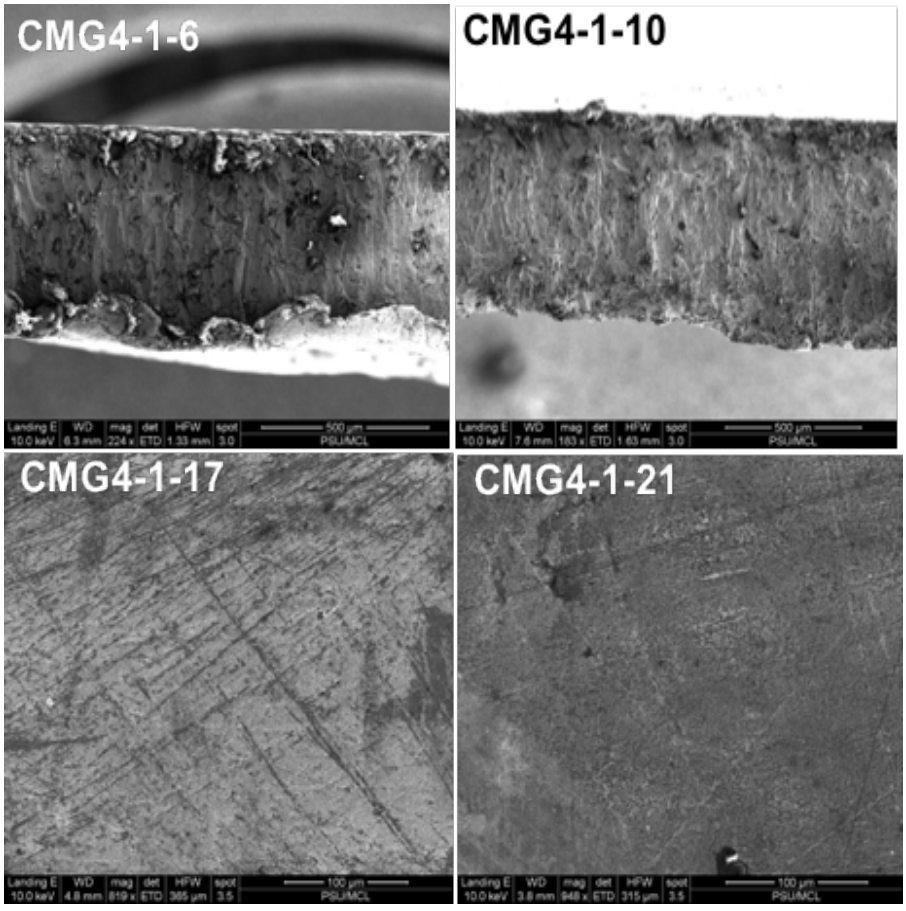

Figure 14. Field emission scanning electron micrographs of representative samples for each of the polished copper specimen

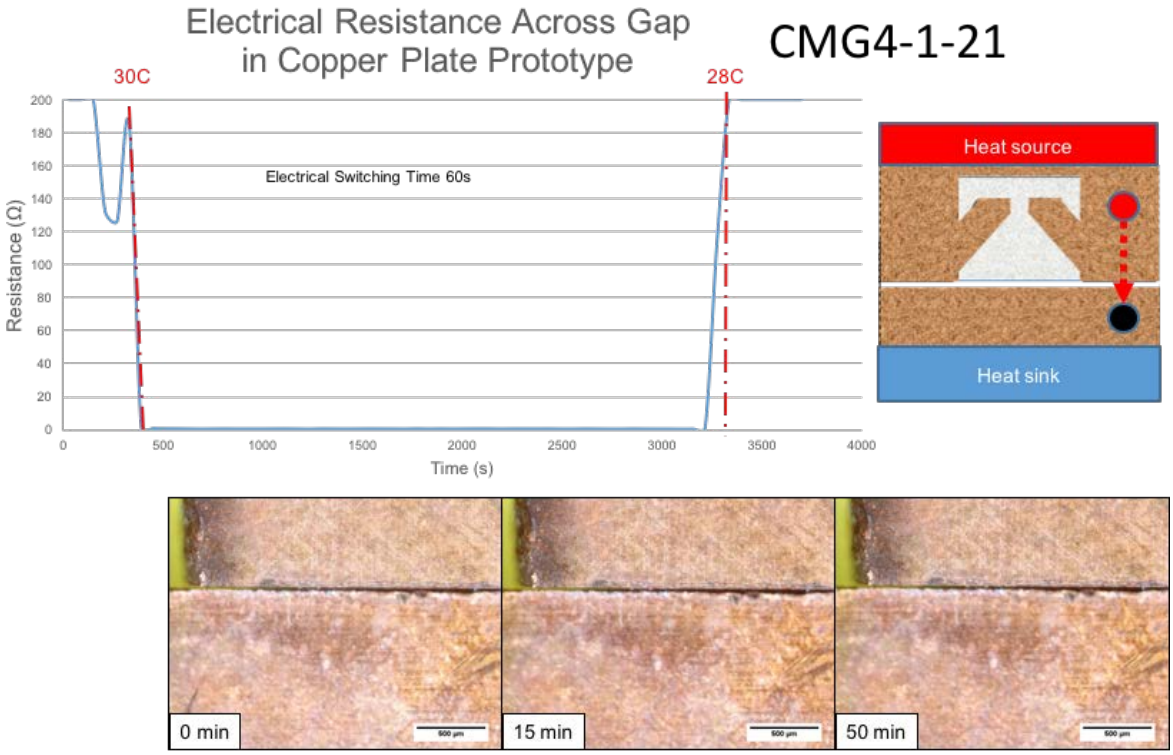

Sample	R_a (μm)	Time for Resistance Decrease to Baseline(s)*
CMG4-1-6	27.6 ± 3.9	ND**
CMG4-1-10	21.7 ± 2.0	300***
CMG4-1-17	4.3 ± 0.8	1020***
CMG4-1-21	1.6 ± 0.5	60

*Upon application of power to thermistor

** Not detected

*** Dropped to a plateau followed by drop to near-zero resistance

Figure 15. Electrical Resistance as a function of time after thermistor start and table of switching time required to reach baseline resistance

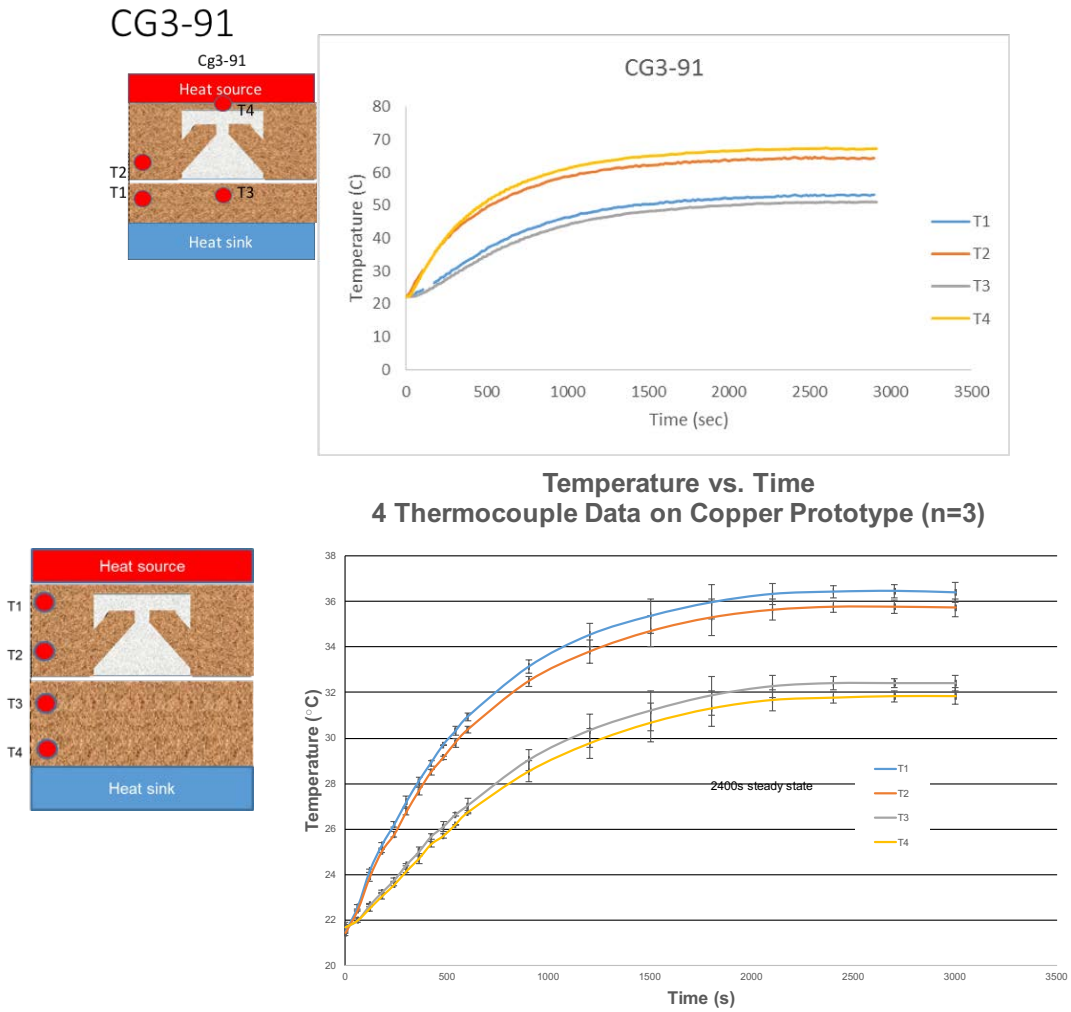

Figure 16. Temperature as a function of time at four thermocouple sites on experimental thermal switch (top) Initial evaluation at large thermistor power and high steady state temperatures (bottom) Thermal evaluation of sample CMG4-1-21

4.2.8 Thermal performance based on Thermal Contact Conductance (TCC)

In the current work, a steady state condition was used to determine experimental thermal contact conductance:

$$Q = -k\frac{dT}{dx} = -k\frac{\Delta(T_2 - T_1)}{\Delta(x_2 - x_1)} \tag{4}$$

where Q is the thermal contact conductance in W/m^2-K, k is the thermal conductivity (401 W/m-K for copper) T_2-T_1 and X_2-X_1 are the temperatures and distance for T3 and T4 in Figure 15 (Bottom) for sample CMG4-1-21.

The Antonetti *et al.* relationship for the theoretical contact conductance, Q, is given by

$$Q = 4200 k_s R_a^{-0.257} \left(\frac{P}{H}\right)^{0.95} \quad (5)$$

where k_s is thermal conductivity (401 W/m-K for copper), P is contact pressure in MPa and H is micro-hardness at approximately 500 MPa for annealed copper. [Poole 1996]

The theoretical TCC in Eq 5 was plotted as a function of contact pressure from 25 MPa to 300 MPa for the four highlighted samples in Figure 13. Eq 5 was used to analyze the temperature change for the four thermal switch samples to determine an experimental thermal contact conductance (Figure 17).

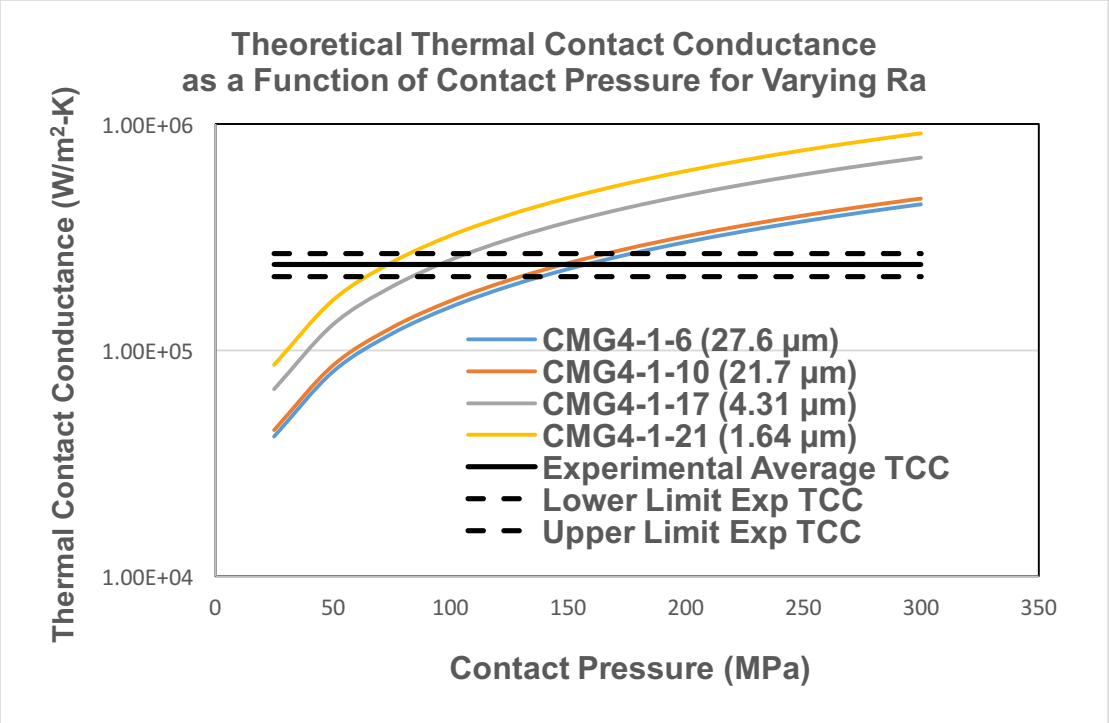

Experimental Thermal Contact Conductance		
Average	**240,000**	**W/m²-K**
Standard Dev	27,500	W/m²-K
Lower Limit (-1sd)	**212,500**	**W/m²-K**
Upper Limit (+1sd)	**267,500**	**W/m²-K**

Figure 17. Theoretical and experimental thermal contact resistance

The theoretical and experimental TCC are relatively consistent, with the lower surface roughness materials achieving a higher TCC at lower contact pressures. Since 200 MPa is the approximate yield strength for copper, cold welding could occur for copper interfaces above this contact stress level. However, the relatively narrow range for the experimental TCC determined for each of the three sets of thermal switches indicate that the experimental and theoretical TCC are relatively consistent.

4.3 Topology optimization using non-dimensional models

Topology optimization is suitable for designing cellular structures with reduced mass and volume and increased performance. A topology optimization approach based on FEM is presented in this section.

4.3.1 SIMP interpolation

The SIMP approach was used to interpolate material properties within an element based on the local design variables, the material densities. The domain is discretized into elements and design variables are associated with each element.

The vector of design variables $\boldsymbol{\rho_0}, \boldsymbol{\rho_1}$ control the quantities of each of two materials (and void) in the domain. In particular, ρ_0 is a density variable controlling the presence of void ($\rho_0 = \rho_{min} \sim 0$) or material ($\rho_0 = 1$). ρ_1 is not strictly a density variable but regulates the presence of one material versus the other: $\rho_1 = 1$ indicates the presence of material 1 while $\rho_1 = 0$ indicates the presence of material 2.

Following the SIMP model, the material properties are interpolated by a smooth and continuous function of the material "densities." For purposes of determining mechanical and thermal response, the effective moduli of elasticity, thermal conductivity, and CTE are determined as follows [Sigmund 2001a, Sigmund 2001b]:

$$\begin{aligned} E(\rho_0^e, \rho_1^e) &= (\rho_0^e)^{p_0}[(\rho_1^e)^{p_1} E_1 + (1-\rho_1^e)^{p_1} E_2] \\ k(\rho_0^e, \rho_1^e) &= (\rho_0^e)^{p_0}[(\rho_1^e)^{p_1} k_1 + (1-\rho_1^e)^{p_1} k_2] \\ \alpha(\rho_0^e, \rho_1^e) &= (\rho_1^e)^{p_1}\alpha_1 + (1-\rho_1^e)^{p_1}\alpha_2 \end{aligned} \tag{6}$$

The penalty term p_0 is set equal to 3, since its role is equivalent to the penalty term used in single material models. p_1, however, is chosen to be equal to 1 if an element contains material, and the material properties of this element are determined by the weighted average of each material property, where the weight is given by the value of ρ_1.

4.3.2 Mechanical contact implementation

The contact model used in this approach assumes that the contact is frictionless and unilateral. In this section, Signorini's contact condition between a body and a fixed boundary are expressed using the approach in [Strömberg & Klarbring 2010] and are smoothed using the formula derived by [Facchinei *et al.* 1999]:

$$\Psi(\xi, \eta) = -\xi + (\xi - \eta)_+ \tag{7}$$

where ξ represents the contact force, η the contact gap between the body and the fixed support, and $(\xi - \eta)_+$ is the function defined as:

$$(\xi - \eta)_+ = \begin{cases} 0 & if\ \xi - \eta \leq 0 \\ \xi - \eta & if\ \xi - \eta > 0 \end{cases} \tag{8}$$

Following these conditions, the displacement at a point A on the body's boundary respects the inequality

$$\boldsymbol{d}^A \cdot \boldsymbol{n}^A - g^A \leq 0 \tag{9}$$

where g^A is the distance from node A to the fixed support, $\boldsymbol{d}^A$ is the displacement vector of node A, and $\boldsymbol{n}^A$ is the direction vector normal to the fixed support surface. Using a finite element formulation, Signorini's contact conditions described in Equations (7) and (8) can be written as:

$$\Psi(\boldsymbol{d}, P_n^A) = -P_n^A + \left(P_n^A + r(\boldsymbol{C}_n^A \boldsymbol{d} - g^A)\right)_+ = 0 \tag{10}$$

where P_n^A represents the contact force at node A, $\boldsymbol{d}$ is the displacement vector and $\boldsymbol{C}_n^A$ is a vector the realizes the scalar product $\boldsymbol{d}^A \cdot \boldsymbol{n}^A$, and r is set to a high value ($\sim 10^7$) for numerical purposes.

4.3.3 Thermo-mechanical governing equations

A two-dimensional, four-node finite element was used to discretize the governing equations. Assume the system is stationary and material behavior is linearly elastic, the discretized thermo-mechanical governing equations take the form

$$\begin{Bmatrix} K_m d + C_n^T P_n - C_{thm} T - F_m \\ \Psi(d, P_n) \\ K_{th} T - F_{th} \end{Bmatrix} = 0 \tag{11}$$

where K_m is the mechanical stiffness matrix, C_{thm} is the thermal expansion coupling matrix, F_p is the mechanical load vector independent from the temperature, K_{th} is the thermal conductivity ("stiffness") matrix, and F_{th} is the thermal load vector. The detailed derivation for each matrix and vector could may be found in [Thurier 2014]. The boundary conditions for a considered thermo-mechanical system is shown in Figure 18.

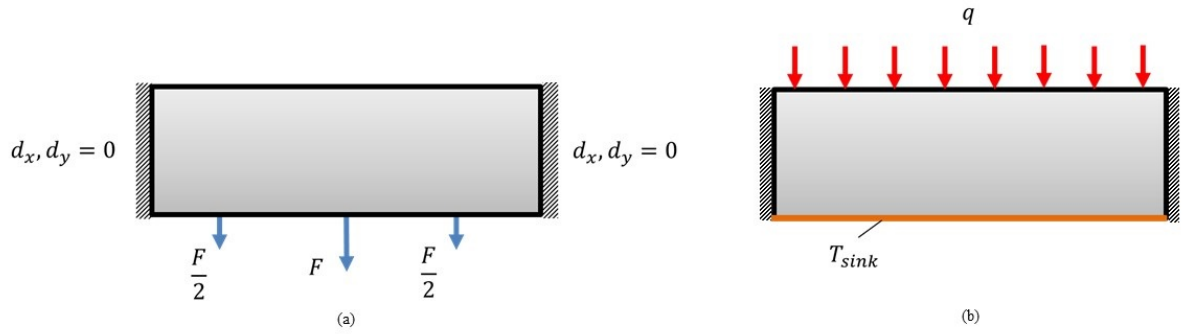

Figure 18. Mechanical and thermal boundary conditions

4.3.4 Implementation of TCR

The TCR model introduced in Section 4.1 was also used here. Using the FEM method and piecewise uniform distribution as shown in Figure 19, the heat flux at the interface is treated as a boundary condition such that, for an element e at the boundary with nodes i and $i+1$:

$$\boldsymbol{K_{th,e}(\rho_e)T_e} = -\frac{ta}{2}\begin{bmatrix} q_i \\ q_{i+1} \\ 0 \\ 0 \end{bmatrix} \tag{12}$$

where $\boldsymbol{T_e}$ is the element temperature vector, t is the thickness of the elements, and a is the semi-length of an element. Substituting $q = \frac{T - T_{sink}}{TCR}$ into Equation (12), it can be written as

$$\boldsymbol{K_{th,e}(\rho_e)T_e} = -\frac{ta}{2}\frac{1}{TCR(P_n)}\begin{bmatrix} T_i - T_{sink} \\ T_{i+1} - T_{sink} \\ 0 \\ 0 \end{bmatrix} \tag{13}$$

Finally, the thermal governing equation is obtained by considering all the elements in the contact region(s):

$$\tilde{K}_{th}T = \tilde{F}_{th} \tag{14}$$

where

$$\tilde{K}_{th} = \sum_e \left(K_{th,e} + \frac{ta}{2TCR(P_n)}\begin{bmatrix} 1 & 0 & 0 & 0 \\ 0 & 1 & 0 & 0 \\ 0 & 0 & 0 & 0 \\ 0 & 0 & 0 & 0 \end{bmatrix} \right) \text{ and } \tilde{F}_{th} = \sum_e \left(F_{th,e} + \frac{taT_{sink}}{2TCR(P_n)}\begin{bmatrix} 1 \\ 1 \\ 0 \\ 0 \end{bmatrix} \right)$$

Then, the governing equations can be rewritten as

$$H = \begin{bmatrix} K_m & C_n^T & -C_{thm} \\ C_n & 1_{nc} & 0 \\ 0 & 0 & \tilde{K}_{th}(P_n) \end{bmatrix}\begin{Bmatrix} d \\ P_n \\ T \end{Bmatrix} - \begin{Bmatrix} F_m \\ g \\ \tilde{F}_{th}(P_n) \end{Bmatrix} = 0 \tag{15}$$

Clearly, the TCR pressure-conductivity model introduces a non-linearity that suggests an iterative method to solving the governing equations. In this approach, the Newton-Armijo Method is used to iteratively solve the equations.

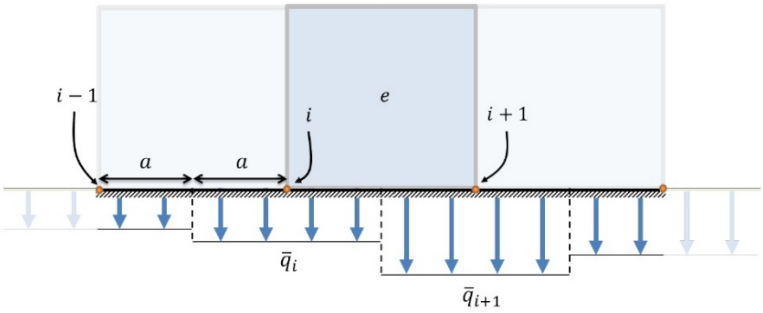

Figure 19. Piecewise uniform distribution of the heat flux at the interface in FEM

4.3.5 Topology optimization algorithm

This section considers the minimization of the "thermal compliance" of the structure. This objective function has the advantage of providing physically interpretable results—that is, not inconsistent with intuition—and usually produces a good numerical response from the algorithm. The objective function consists of the matrix product of the temperature and the thermal stiffness matrix such that

$$c_0(\boldsymbol{\rho_0}, \boldsymbol{\rho_1}) = \boldsymbol{T}^T \boldsymbol{K_{th}} \boldsymbol{T} \tag{16}$$

and the sensitivities are given by

$$\frac{\partial c_0}{\partial \rho_i}(\boldsymbol{\rho_0}, \boldsymbol{\rho_1}) = \boldsymbol{T}^T \frac{\partial \boldsymbol{K_{th}}}{\partial \rho_i}(\boldsymbol{\rho_0}, \boldsymbol{\rho_1}) \boldsymbol{T} \tag{17}$$

To address potential checkerboard problems, which involve solutions that contain regions of adjacent elements with alternating void and material, the sensitivities are filtered using the technique proposed by [Andreassen *et al.* 2011]

$$\frac{\partial \widehat{c_0}}{\partial \rho_0^e}(\rho_0^e, \rho_1^e) = \frac{1}{\max(\rho_{min}, \rho_0^e) \sum_{i=1}^N \widehat{H}_i} \sum_{i=1}^N \widehat{H}_i \, \rho_0^i \frac{\partial c_0}{\partial \rho_0^i} \tag{18}$$

$$\frac{\partial \widehat{c_0}}{\partial \rho_1^e}(\rho_0^e, \rho_1^e) = \frac{1}{\sum_{i=1}^N \widehat{H}_i} \sum_{i=1}^N \widehat{H}_i \frac{\partial c_0}{\partial \rho_1^i} \tag{19}$$

where the convolution operator $\widehat{H} = \max(0, r_{min} - \Delta(e,i))$, $\Delta(e,i)$ represents the distance between a specific element e and its neighbor i, and the parameter r_{min} defines the size of the neighborhood of this element e.

Figure 20 shows a flowchart of the algorithm, which is summarized as follows:

1. Formulate an initial guess for the design variables $(\boldsymbol{\rho_0}, \boldsymbol{\rho_1})$
2. Formulate an initial guess for $\boldsymbol{x}$
3. Solve the governing equations using the Newton-Armijo Method
4. Calculate and filter the sensitivities
5. Update the design variables using Method of Moving Asymptotes (MMA) [Svanberg 1987]
6. If changes in the design variables are observed, return to step 2 using the updated design variables.

If the change in all design variables is smaller than some threshold (say 1%), the algorithm stops, and the topology is considered to be optimal.

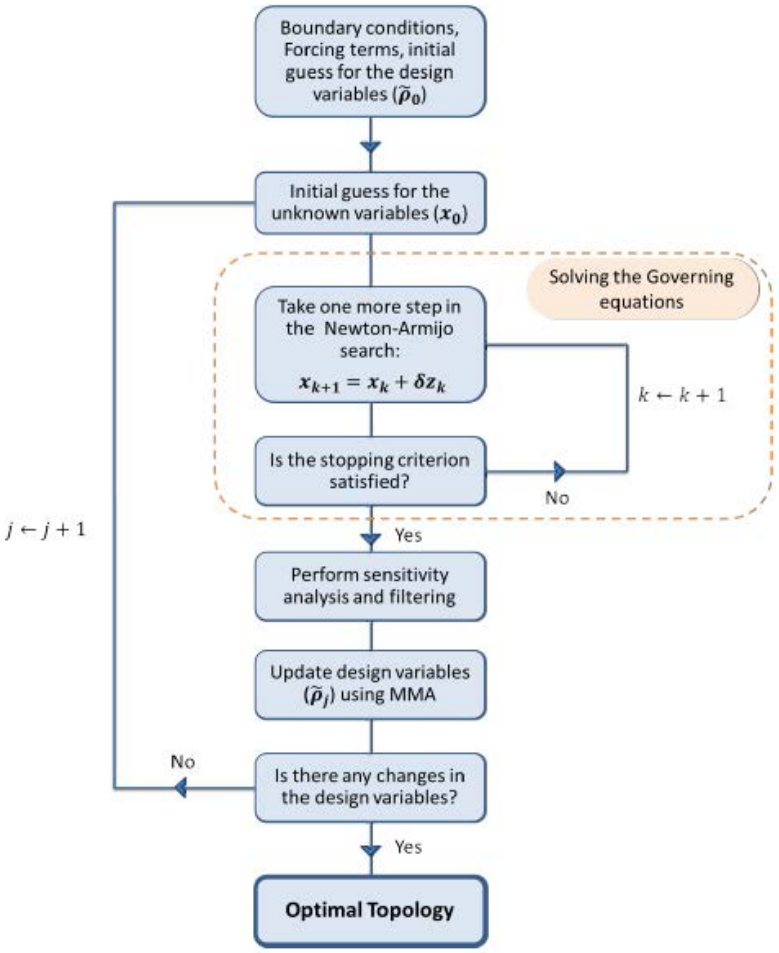

Figure 20. Flowchart of the topology optimization algorithm

4.3.4 Optimization results

In a first example case, the mechanical behavior of the structure is not considered, and a uniform contact pressure is assumed at the interface. The value of the TCR was adjusted to study its effect on a thermally-based optimum design. The parameter values used in these simulations are given in Table 2 and the boundary conditions are shown in Figure 21(b).

This geometry is symmetric, and several optima are likely to be close together in the space of solutions for the design variables. In such a case, the initial guess could be important. In this approach, the initial guess for the design variables is a uniform distribution, in which every element contains some "void," and some "material." Arc-like structures are obtained in each topology presented in Figure 10, with the highly conductive material (in red) placed in the center. Also, good contact ($TCR = 1$) results in more direct heat-conductive paths between the two boundaries than other configurations. This case can be considered "ideal" contact, where the temperature boundary condition corresponds to a prescribed temperature $T \approx Tsink$, as the temperature profile within the structure suggests (Figure 22(d)). Higher TCR values tend to increase the average temperature of the structure and force placement of material near the contact boundary (Figures 22(b) & (c) and their temperature profiles in Figure 22(e) & (f) respectively).

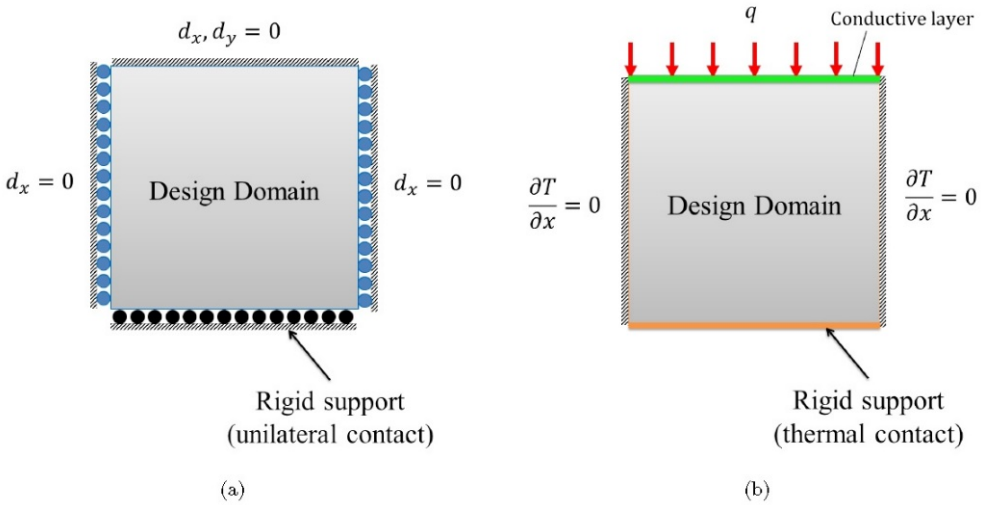

Figure 21. Mechanical and thermal boundary conditions of the topology optimization problem

Table 2. Standard values for the parameters in C3M designs

Conductivity of material 1	k_1	2
Conductivity of material 2	k_2	1
Reference Temperature	T_{ref}	0
Sink Temperature	T_{sink}	10
Heat flux input	q	1
Volume fraction of void	$1 - f_0$	0.6
Volume fraction of material 1	$f_0 \times f_1$	0.2
Volume fraction of material 2	$f_0(1 - f_1)$	0.2
Filter's radius	r_{min}	1.2
Mesh Resolution	$n_x \times n_y$	50×50

In a second example case, the topologies presented were obtained using a thermo-mechanical model with contact. The only mechanical loading on the structure comes from thermal expansion. Under hot temperature conditions (above T_{ref}), the structure generally expands, but is constrained within the space defined by the lateral boundary conditions presented in Figure 21(a). Therefore, contact is made at the bottom boundary. The thermal boundary conditions used are given in Figure 21(b), and the values of the parameters used in the simulations are given in Table 3. Again, the objective was minimization of the thermal compliance of the structure.

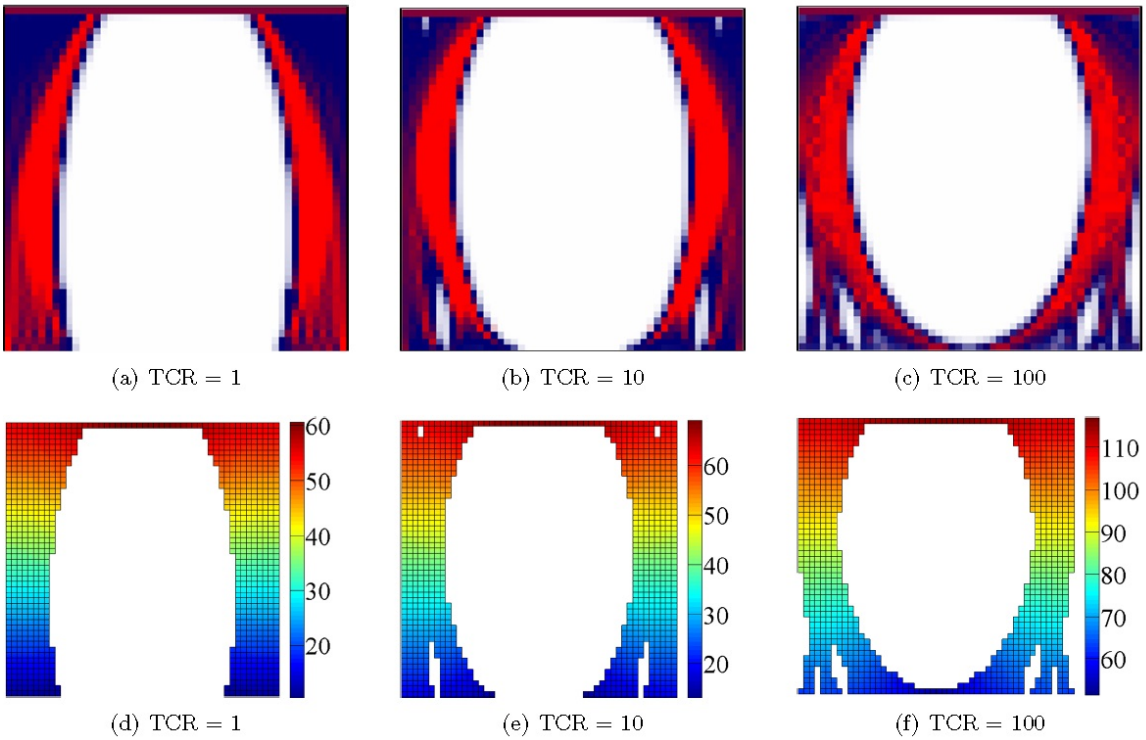

Figure 22. Minimum thermal compliance topologies depending on the change in the TCR at the bottom boundary and the corresponding temperature distribution within the solid structure

Table 3. Standard values for the parameters using a thermos-mechanical model with contact

Modulus of elasticity of material 1	E_1	2
Modulus of elasticity of material 2	E_2	2
Conductivity of material 1	k_1	2
Conductivity of material 2	k_2	1
CTE of material 1	α_1	5×10^{-4}
CTE of material 2	α_2	2×10^{-4}
Poisson ratio	ν	0.3
Reference Temperature	T_{ref}	0
Sink Temperature	T_{sink}	0
Heat flux input	q	0.5
Volume fraction of void	$1-f_0$	0.5
Volume fraction of material 1	$f_0\times f_1$	0.2
Volume fraction of material 2	$f_0(1-f_1)$	0.3
Filter's radius	r_{min}	1.2
Mesh Resolution	$n_x\times n_y$	30×30

Figure 23 shows that for high values of the TCR (or low values for h_{c0}), the high conductivity material is placed near the heat flux boundary. The results are similar to those obtained using the thermal model in the first case. Also, when the volume fraction of each material is not constrained, the material with the higher conductivity tends to be chosen, and the other abandoned, even for a high mismatch in the CTEs. This result suggests that the objective function is relatively insensitive to the thermal contact condition at the bottom, and therefore could be reconsidered.

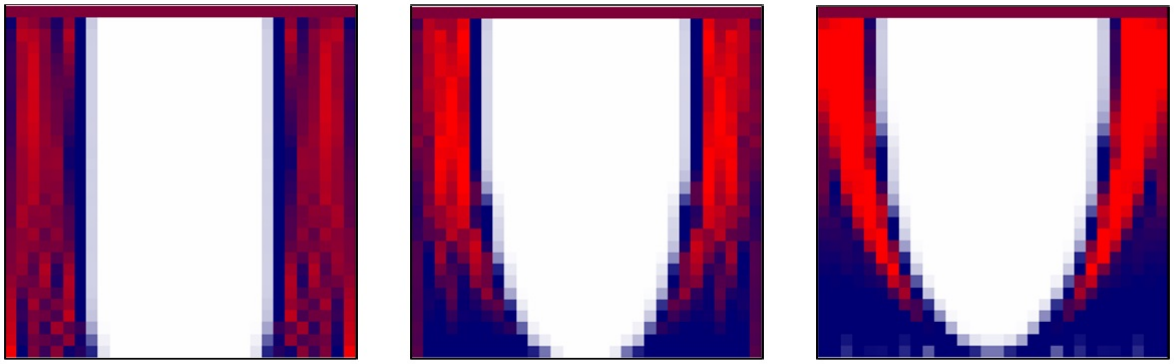

(a) $h_{c0} = 1$ (b) $h_{c0} = 0.1$ (c) $h_{c0} = 0.01$

Figure 23. Optimal designs for a thermal compliance optimization problem using different h_{c0}

4.3.5 Fabrication of optimized cells

As previously noted, the use of LM-RIF was largely invalidated by the current work. The major limitation of LM-RIF is the need to use nanometer scale particles. However, based on the relatively forgiving high TCC achieved even with metal contact interfaces exhibiting large surface roughness, the use of other additive manufacturing approaches to fabricate thermal switches should be considered. In preliminary 3D printing, a two-color PLA was used to mimic one of the optimal designs (Figure 24). Future 3-D additive fabrication methods could conceivably keep pace with the elegance of the complex material and geometric designs being created. Further 3D printing efforts are summarized in an Appendix.

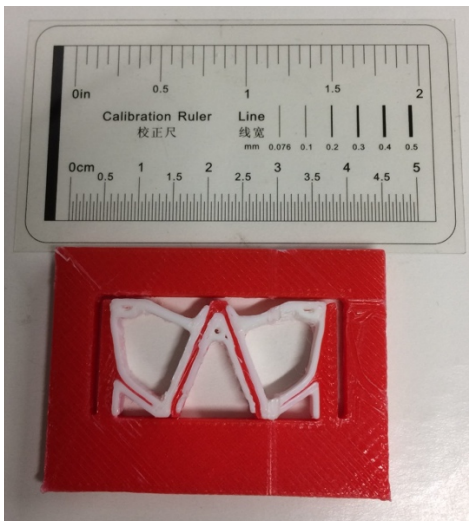

Figure 24. Two-material complex design created with a two-color PLA filament 3D printer

4.4 Topology optimization using real dimensional models

In this section, realistic parameter values are used in the model to generate optimal topologies for structures capable of satisfying project research objectives. As suggested in Section 4.2, the C3M structure exhibits less of a discrete step-change (thermal "switch") between high- and low-conducting modes and more of a continuous change modulated by contact pressure (thermal "valve"). Therefore, an assumption of consistent continuous contact is made for the model addressed in this section.

4.4.1 1-D model

A one-dimensional model was created to assess the validity of the always-contact assumption as shown in Figure 25. Another goal of the 1-D model was to determine a suitable difference between T_{ref} and T_{sink}, namely $T_{sink} - T_{ref}$. The reference temperature T_{ref} is defined as the temperature at which the free thermal strain is zero. In other words, if the whole device has a constant temperature T_{ref}, the contact pressure is zero. And T_{sink} is defined as the sink temperature.

First, the governing equation of the steady-state thermal system can be written as:

$$qA = k\frac{A}{L}\Delta T = k\frac{A}{L}(T_{top} - T_{bot}) \tag{20}$$

where q is the input heat flux, A is the cross sectional area, L is the thickness of the cell, T_{top} is the temperature at the top boundary, and T_{bot} is the temperature at the bottom boundary. Then T_{bot} can be derived in terms of T_{top}:

$$T_{bot} = T_{top} - \frac{qL}{k} \tag{21}$$

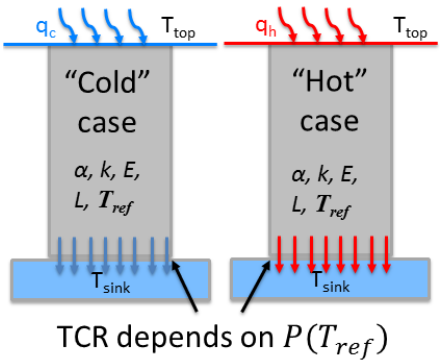

Figure 25. 1-D always-contact model

Assuming that the system is in a steady state, the heat flux through the contact interface is equal to the input heat flux. The temperatures across the contact interface are substantially different. Substituting Equation (1) into Equation. (21) yields

$$T_{top} = q\left(\frac{L}{k} + TCR\right) + T_{sink} \tag{22}$$

Now, considering the mechanical system, based on linear thermal expansion, the free thermal strain in the cell is:

$$\varepsilon = \alpha\left[\frac{1}{2}\left(T_{top}+T_{bot}\right)-T_{ref}\right] = \alpha\left(T_{top}-T_{ref}-\frac{qL}{2k}\right) \tag{23}$$

where α is the thermal expansion coefficient. Since mechanical displacements are restricted at the top and bottom, the contact pressure is equal to the thermal stress:

$$p = \sigma = E\varepsilon = E\alpha\left(T_{top}-T_{ref}-\frac{qL}{2k}\right) \tag{24}$$

Recalling the TCR model, substituting Equation (24) and (2) into Equation (22) yields an ultimate form of the governing equation for the 1-D system

$$T_{top}-\frac{qR_a^{0.257}}{4200k_s(E\alpha)^{0.95}}\left(\frac{T_{top}-T_{ref}-\frac{qL}{2k}}{H}\right)^{-0.95}-\left(T_{sink}+\frac{qL}{k}\right)=0 \tag{25}$$

Using the parameter values shown in Table 4, a parametric study was made by varying the input heat flux and sink temperature. The goal was to find a range of values for T_{sink} and to select a material such that the top temperature remains in a specific temperature range under various heat input (β from 0.05 to 2). (β is the heat input factor, q = 5×10^4W/m^2 when $\beta = 1$. The higher β, the higher heat input.)

Table 4 Parameter values for the 1-D model

Input Parameters	Value	Material Properties	Value	Contact Parameters	Value
T_{ref}	295K	E	120GPa	k_s	401W/(m·K)
T_{sink}	$[285K, 305K]$	k	401W/(m·K)	R_a	1μm
q_h	5×10^4W/m^2	α	1.65×10^{-5}	H	(E/120GPa)*5GPa
q	$q = \beta q_h$, $\beta \in [0.05,2]$	L	0.025m		

Figure 26 shows a contour plot for the bottom temperature, top temperature, the temperature difference between the contact interface and the contact pressure. The x axis represents the temperature difference between T_{sink} and T_{ref}, and the y axis represents the heat input factor β. When $T_{sink}-T_{ref}>0$, $\Delta T_{interface}$ is very small (less than 1K), and $\frac{\partial \Delta T_{interface}}{\partial \beta}$ is also very small. In this 1-D model, T_{top} is the key characteristic of the C3M device. An ideal performance of the C3M device is that T_{top} remains constant while the input heat flux is increasing or decreasing, which suggests that $\left|\frac{\partial T_{top}}{\partial \beta}\right|$ should be designed to be as small as possible.

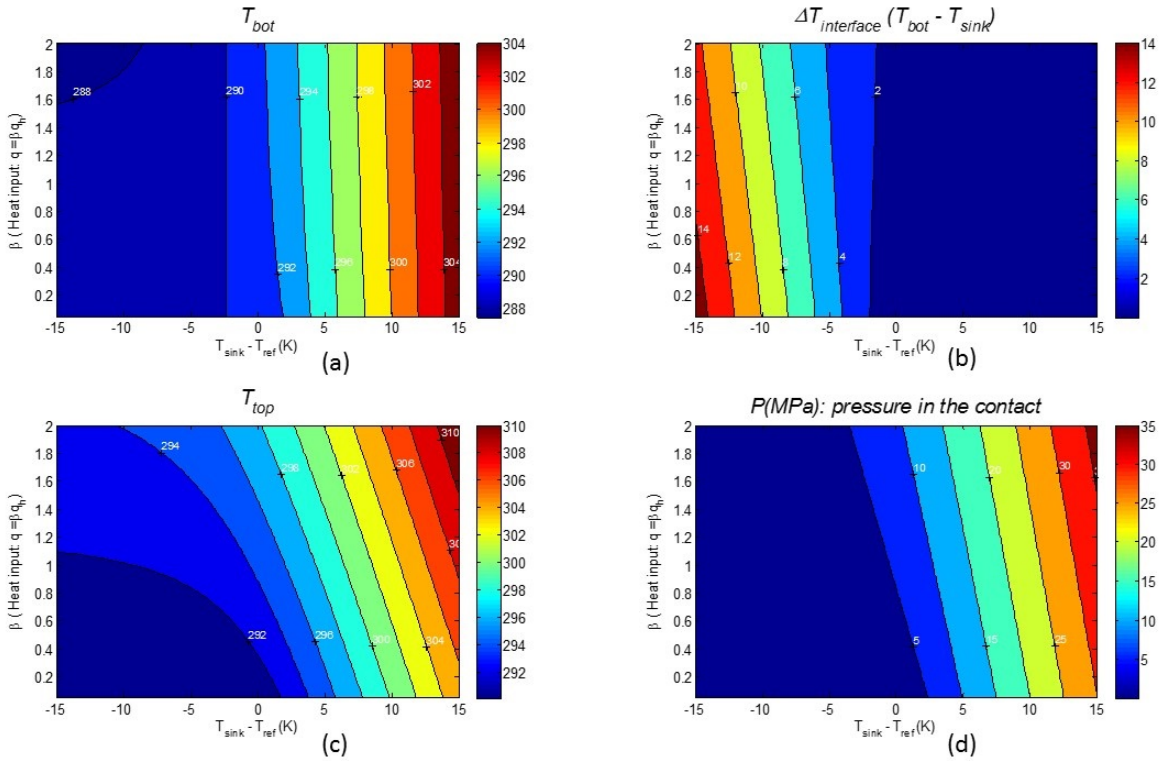

Figure 26. Contour map results from the 1-D model

As seen in Figure 26, when $T_{sink} - T_{ref} < 0$, $\Delta T_{interface}$ increases as T_{sink} decreases. Also, T_{top} is much lower than that when $T_{sink} - T_{ref} > 0$, and $\left|\frac{\partial T_{top}}{\partial \beta}\right|$ is lower than that when $T_{sink} - T_{ref} > 0$. Therefore, a reasonable conclusion is that $T_{sink} < T_{ref}$ is suitable for the C3M device under the always-contact assumption. And under such a condition, the always-contact assumption is feasible to design a passive C3M thermal control device.

Note that T_{top} is always higher than T_{sink} because of the always-contact assumption. Therefore, selecting a T_{sink} equal or higher than the minimum allowable temperature of the electronic device would guarantee the top surface of the cell never dropping below the cold limit. (This might not always be possible in practice.)

4.4.2 2-D model GDE solver

The 2-D problem addressed here is the same as the one described in Section 4.3 and shown in Figure 21. The same 2-D FEM technique was used to discretize the nonlinear thermo-mechanical governing equations. However, in this approach, an initial set of bottom nodal temperatures was assumed, so that the thermal governing equations $\{F_{th}\} = [K_{th}]\{T\}$ can be solved easily. This yields a trial solution $\{T(x, y)\}$ for the temperature distribution in the cell.

The nodal pressure at the bottom interface, denoted as p_{th}, can be determined from the bottom nodal temperature and the TCR expression. Substitution of the trial temperature solution into the mechanical governing equations yields the full solution of the thermo-mechanical equations. The bottom nodal pressure, p_m, can be also separately determined from the solution of these

mechanical governing equations. If the initial "guess" for the bottom interface temperature was correct, p_{th} should be equal to p_m. Therefore, solving the nonlinear governing equations is equivalent to solving:

$$\boldsymbol{p_{th}(T_{bot}) - p_m(T_{bot}) = 0} \tag{26}$$

Define a bottom node index for the thermal discretized governing equations:

$$i = 1,2,\dots,nelx+1;\ j = 1,2,\dots,nelx+1$$

and a global node index:

$$k = i\times(nely+1);\ l = j\times(nely+1)$$

where $nelx$ is the total element number in the x direction, and $nely$ is the total element number in the y direction. And the set of all the DOFs is denoted $alldofth$, and the set of free DOFs as $freedofth$. For the bottom nodes:

$$\frac{F_{th}(k)}{2a} = \frac{T(k)-T_{sink}}{TCR} = \frac{T(k)-T_{sink}}{\xi p} \tag{27}$$

where a is the semi-length of the element, p is the nodal pressure, and $\xi = TCC_0 = 4200k_sR_a^{-0.257}/H$ is a parameter that depends on the condition of the contact surface. Thus, the nodal pressure can be expressed as a function of the nodal temperature as follows:

$$p_{th}(i) = \frac{F_{th}(k)}{2\xi a(T(k)-T_{sink})} \tag{28}$$

The derivative of the nodal stress subject to the nodal temperature is

$$\frac{\partial p_{th}(i)}{\partial T(j)} = \frac{\partial\left[\frac{F_{th}(k)}{2\xi a(T(k)-T_{sink})}\right]}{\partial T(l)} = \frac{K_{th}(k,l)}{2\xi a(T(k)-T_{sink})} - \delta_{kl}\frac{F_{th}(k)}{2\xi a(T(k)-T_{sink})^2} \tag{29}$$

where $\delta_{kl} = \begin{cases}0, if\ k \neq l\\ 1, if\ k = l\end{cases}$

For the mechanical system, denote the index for the bottom DOF in the y direction:

$$kk = 2i\times(nely+1)$$

The governing equation of the discretized mechanical system is shown in matrix form as:

$$\{F\} = [K]\{d\} \tag{30}$$

where $\{F\}$ is the generalized mechanical force vector, $[K]$ is the elastic stiffness matrix, and $\{d\}$ is the displacement vector. Now, denote the set of restrained DOFs as $fixeddofel$, and the set of free DOFs as $freedofel$. Hence, the vertical restrained forces at the bottom nodes are

$$R_y(i) = F(kk) = \sum_{m}^{freedofel} K(kk,m)d(m) \tag{31}$$

The displacement in terms of the temperature in the matrix form can be described as

$$\left[K_{freedofel}\right]\left\{d_{freedofel}\right\} = [C]\{T\} - \{C_{ref}\}T_{sink} \tag{32}$$

where $[C]$ and $\{C_{ref}\}$ are the thermo-mechanical coupling matrix. Hence,

$$\left\{d_{freedofel}\right\} = \left[K_{freedofel}\right]^{-1}[C]\{T\} - \left[K_{freedofel}\right]^{-1}\{C_{ref}\}T_{sink} \tag{33}$$

Defining$[M] = \left[K_{freedofel}\right]^{-1}[C]$, the derivative of the displacement subject to the temperature is

$$\frac{\partial d(m)}{\partial T(p)} = \frac{\partial d_{freedofel}(n)}{\partial T(p)} = M(n,p) \tag{34}$$

where $m = 1,2,\dots,2(nelx+1)(nely+1)$, $n \in freedofel$, $p \in alldofth$. Define a function $ID8$, such that $n = ID8(m)$. Note that $ID8(kk) = 0$. Also the bottom nodal pressure can be derived from the mechanical governing equation as:

$$p_m(i) = F(kk)/(2a) \tag{35}$$

The derivative of the nodal pressure subject to the nodal temperature is (using chain rule)

$$\frac{\partial p_m(i)}{\partial T(j)} = \frac{1}{2a}\frac{\partial F(kk)}{\partial T(l)} = \frac{1}{2a}\sum_{m}^{freedofel} K(kk,m)\sum_{p}^{alldofth} M(ID8(m),p)\frac{\partial T(p)}{\partial T(l)} \tag{36}$$

Recalling the thermal governing equation, the Dirichlet boundary conditions has contributions in the thermal force vector, which implies that

$$\frac{\partial T(p)}{\partial T(l)} = \begin{cases} \sum_{q}^{freedofth} \frac{\partial T(p)}{\partial F_{th}(q)}\frac{\partial F_{th}(q)}{\partial T(l)} = \sum_{q}^{freedofth} \widetilde{K}_{th}(p,q)\frac{\partial F_{th}(q)}{\partial T(l)} & if\ p \in freedofth \\ \delta_{pl} & otherwise \end{cases} \tag{37}$$

Note that the Dirichlet boundary condition $T(l)$ only contributes to the elements that involve Node l.

$$\frac{\partial F_{th}(q)}{\partial T(l)} = \begin{cases} -k^e(4,2) & q = l - nely - 2 \\ -k^e(3,1) & q = l + nely \\ -k^e(4,1) & q = l - 1 \;\&\; l = nely + 1 \\ -k^e(3,2) & q = l - 1 \;\&\; l = (nelx + 1)(nely + 1) \\ -k^e(4,1) - k^e(3,2) & q = l - 1 \;\&\; l \neq nely + 1 \;\&\; l \neq (nelx + 1)(nely + 1) \\ 0 & otherwise \end{cases} \tag{38}$$

where k^e denotes the element thermal stiffness matrix. Therefore,

$$\frac{\partial p_m(i)}{\partial T(j)} = \begin{cases} \frac{1}{2a} \sum_{m}^{freedofel} K(kk,m) \sum_{p}^{alldofth} M(ID8(m),p) \sum_{q}^{freedofth} \widetilde{K}_{th}(p,q) \frac{\partial F_{th}(q)}{\partial T(l)} & if\ p \in freedofth \\ \frac{1}{2a} \sum_{m}^{freedofel} K(kk,m) \sum_{p}^{alldofth} M(ID8(m),p)\, \delta_{pl} & otherwise \end{cases} \tag{39}$$

From Equations (28) and (35), the value of $\boldsymbol{p_{th} - p_m}$ can be obtained. And from Equation (29) and (39), the derivative of $\boldsymbol{p_{th} - p_m}$ subject to $\boldsymbol{T_{bot}}$ can be developed. A Newton method was used to solve Equation (26) and, equivalently, the governing equations.

4.4.3 Topology optimization algorithm

An objective function was defined having a direct relationship to the design goals: namely, minimizing the average temperature of the top surface under the maximum heat flux, q = 5×10^4W/m^2.

$$c_0(\boldsymbol{\rho_0}, \boldsymbol{\rho_1}) = \frac{\sum \boldsymbol{T_{top}}}{nelx + 1} \tag{40}$$

Assuming that a small change in ρ_i does not change T_{bot} appreciably, the *approximate* sensitivity of T_{top} subject to ρ_i can be derived directly from the thermal governing equation

$$\frac{\partial\{T\}}{\partial \rho_i} = \frac{\partial[K_{th}]^{-1}}{\partial \rho_i}\{F_{th}\} = -[K_{th}]^{-1}\frac{\partial[K_{th}]}{\partial \rho_i}[K_{th}]^{-1}\{F_{th}\} \tag{41}$$

Therefore the sensitivity of the objective function can be approximated as

$$\frac{\partial c_0}{\partial \rho_i}(\boldsymbol{\rho_0}, \boldsymbol{\rho_1}) = -\frac{1}{nelx + 1}\sum\left([K_{th}]^{-1}\frac{\partial[K_{th}]}{\partial \rho_i}[K_{th}]^{-1}\{F_{th}\}\right)_{top} \tag{42}$$

where the subscript top indicates the index of the top nodes in the FEM formula.

Figure 27 provides a flowchart of the algorithm. If the change in all design variables is less than 1%, the algorithm stops, and the topology is considered to be an optimum.

4.4.4 Results and discussion

Table 5 summarizes the parameter values used in the optimization. Three materials, Copper, Aluminum and Zirconia, were used in the topology optimization.

Table 5. Parameters value for 2D topology optimization

Modulus of elasticity of Copper	E_1	$120GPa$
Modulus of elasticity of Aluminum	E_2	$70GPa$
Modulus of elasticity of Zirconia	E_3	$200GPa$
Conductivity of Copper	k_1	$401W/(mK)$
Conductivity of Aluminum	k_2	$167W/(mK)$
Conductivity of Zirconia	k_3	$2.7W/(mK)$
CTE of Copper	α_1	16.5×10^{-6}
CTE of Aluminum	α_2	22.2×10^{-6}
CTE of Zirconia	α_3	10.1×10^{-6}
Poisson ratio	ν	0.3
Reference Temperature	T_{ref}	$290K$
Sink Temperature	T_{sink}	$275K$
Heat flux input	q	$50000W/m^2$
Filter's radius	r_{min}	1.2
Size of design domain	$A\times L$	$75mm\times25mm$
Mesh Resolution	$n_x\times n_y$	30×10

The first example case is a topology optimization problem based on using a single material, Copper. To ensure that the two sides of a conducting interface are always in contact, a bottom layer with one element thickness is fixed (non-design) in the optimization. A top layer is also fixed to distribute the input heat flux appropriately and decrease any temperature variance on the top surface.

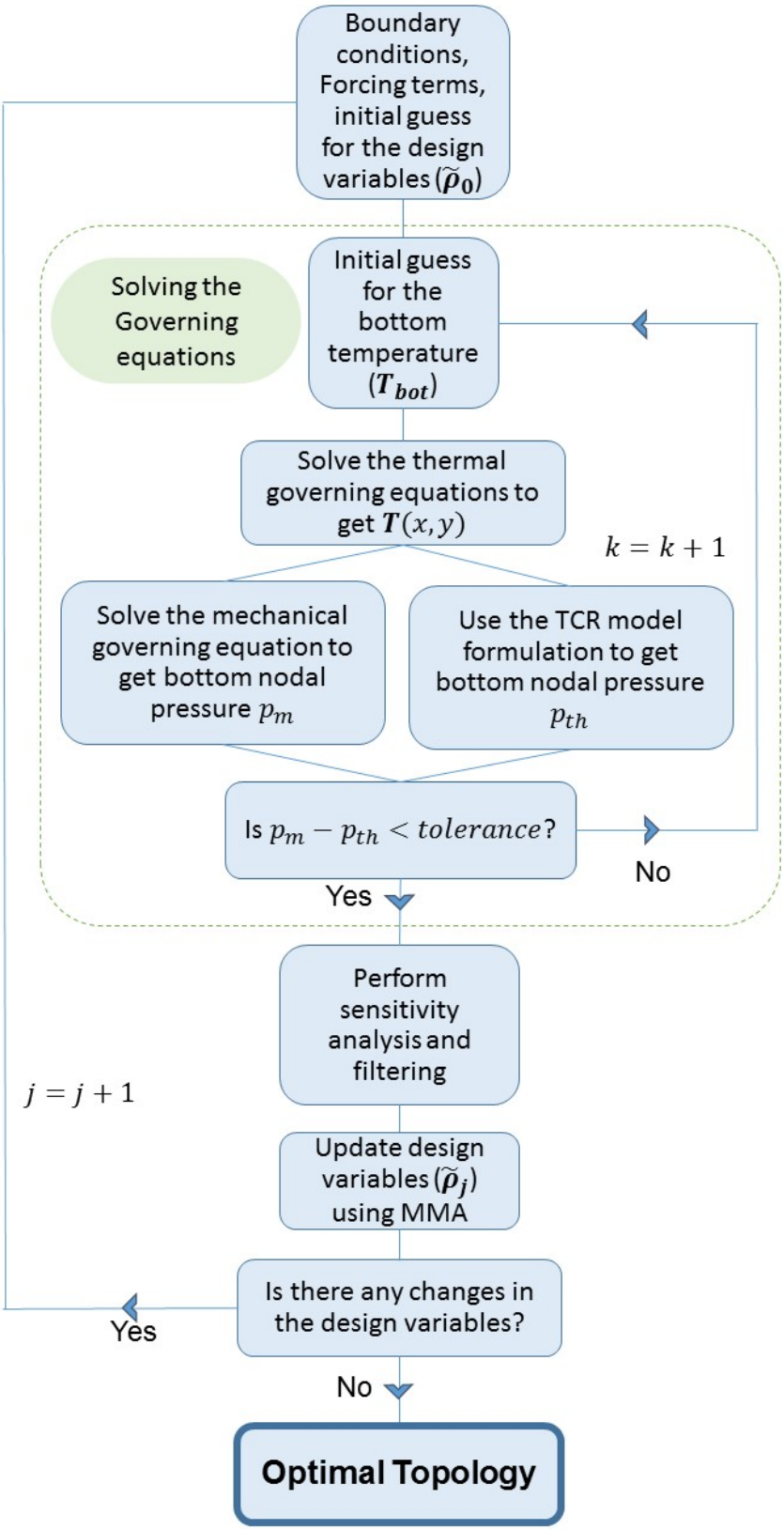

Figure 27. Flow chart of topology optimization of an "always-contact" model

Figure 28 shows an optimal solution topology (black represents material), temperature distribution and bottom nodal stress: (a) shows the results with volume fraction $\rho_0 = 0.6$, while (b) shows the results with $\rho_0 = 0.4$. Both topologies look similar to those in Figure 23: material is concentrated at the left and right boundaries, with a central void. The bottom stresses are concentrated at the corners, which leads to the lowest temperature in the entire design domain.

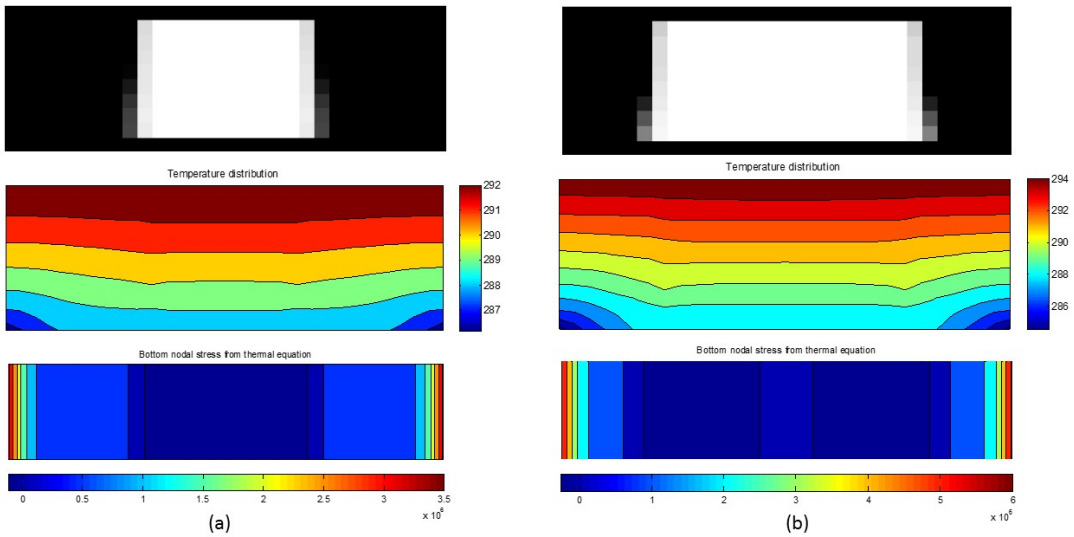

Figure 28. One-material topology optimization with fixed top layer

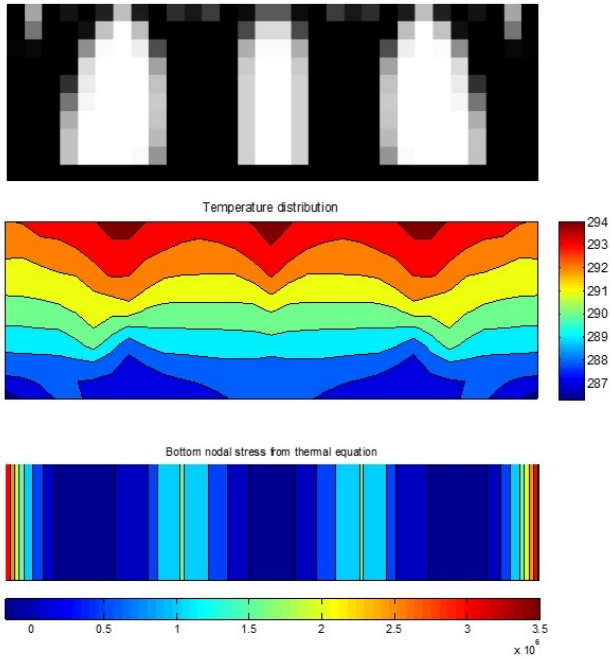

Figure 29. One-material topology optimization without fixed top layer

The second example case is also based on a single material, Copper, with volume fraction $\rho_0 = 0.6$. But the fixed top layer is removed, it becomes a free design region. The topology, temperature distribution and bottom nodal stress of the optimal results are shown in Figure 29. The topology looks somewhat different from that in Figure 28.

The third example case involves the use of two materials, Copper and Aluminum, with volume fraction $\rho_0 = 0.6$. The topology, temperature distribution and bottom nodal stress of the optimal results are shown in Figure 30: (a) shows the results with Copper volume fraction $\rho_0\rho_1 = 0.5$, while (b) shows the results with Copper volume fraction $\rho_0\rho_1 = 0.2$. Red represents Copper and blue represents Aluminum. Note that Figure 30(b) shows features similar to those in Figure 22, namely the highly conductive material (in red) placed in the center of the design.

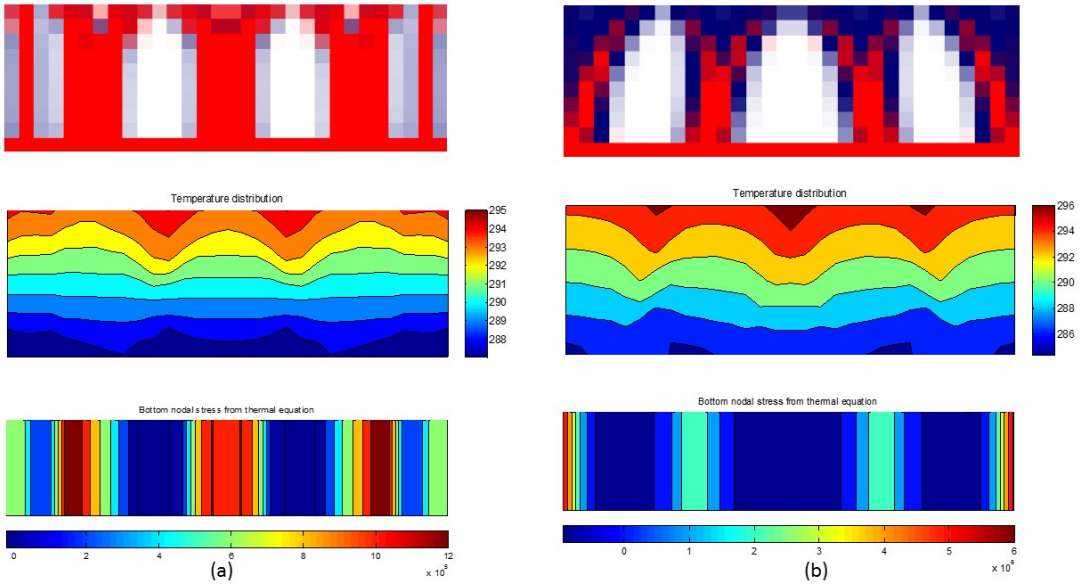

Figure 30. Two-material topology optimization without fixed top layer

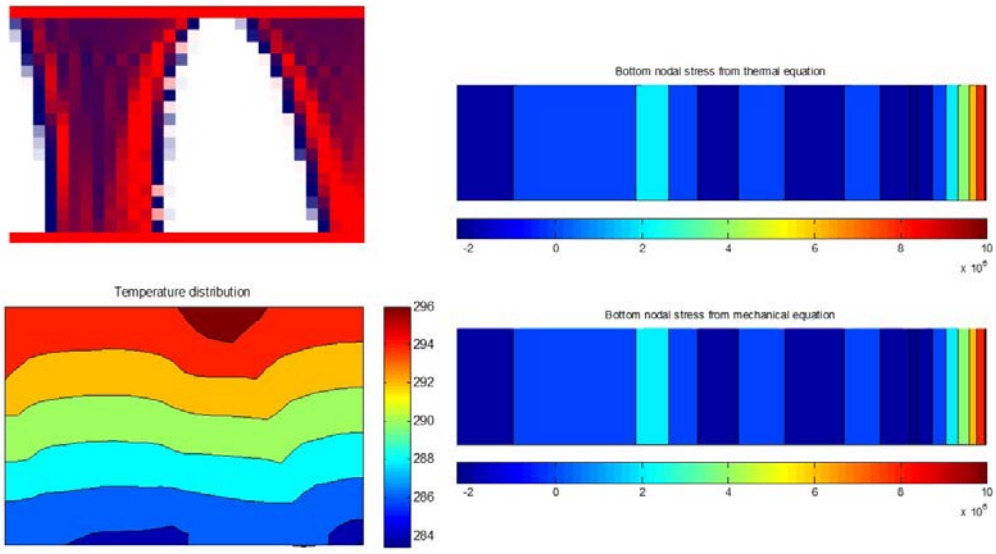

Figure 31. Two-material topology optimization with fixed top layer

A final example case is again based on two materials, Copper and Zirconia, with the volume fraction $\rho_0 = 0.6$. A top layer made of Copper is fixed in the design domain. The resolution is doubled in each dimension, 60×20. Because of the symmetry of the design domain, to reduce computational time only half needs to considered. Therefore, the resolution used is 30×20. The semi-topology, temperature distribution and bottom nodal stress of the optimal results are shown in Figure 31: the Copper volume fraction is $\rho_0\rho_1 = 0.3$, while the Zirconia volume fraction is $\rho_0(1-\rho_1) = 0.3$.

One weakness of the method is that the bottom nodal stress distribution can occasionally indicate negative normal stresses at the contact interface, indicating violation of the "always-contact" assumption. (Alternatively, it might indicate a negative TCR which also violates basic physics principles.) Furthermore, if too small a volume fraction ρ_0, is considered, convergence might not be achieved. These conditions indicate that the algorithm, while generally effective, lacks certain robustness. This could perhaps be improved in future research.

5. Conclusions

Thermal management of electronic "black boxes" is a major concern in spacecraft systems. Passive thermal control is preferred over active control because of high reliability and the potential for reduced overall weight. In this research, the C3M concept was adopted and pursued to passively control heat transfer from source electronics to a radiating exterior surface. These C3M structures employ thermally-driven deformation to create or break contact or to modify the contact pressure and thereby control heat conduction through the contact interface. This represents a novel approach to passive thermal control.

In early research, a proposed bi-material T-shaped cell was modeled using the finite element method and subjected to thermal loads representative of those experienced by typical spacecraft equipment. A TCR model was adopted to study thermal conduction across a contact interface. The interface TCR depends strongly on the normal pressure acting at the interface, which makes the contact system exhibit a more gradual change between insulating and fully-conducting modes, unlike conventional thermal switches. Simulation results obtained using ANSYS showed that the cell was able to meet a high-conductivity goal under high thermal loading and change to a low conductivity (less than $1/20^{th}$ of the high-conductivity value) under low thermal loading.

In continuing design research, a topology optimization approach was developed to optimize the thermal performance of a C3M contact structure. Based on a 2D finite element formulation and Solid Isotropic Material with Penalization (SIMP) interpolation for material properties, the topology optimization method was used to determine the distribution of two distinct materials in the C3M cells. The Method of Moving Asymptotes (MMA) was used as the optimization scheme for determining the design variables. The objective function used was the global mechanical / thermal compliance of the structure. A thermal contact model based on unilateral contact used a Newton method to solve the nonlinear governing equations. Results for one-material and two-material models showed the ability of the design algorithm to generate patterns and features that could be used in a future system. A structure with arc-like features was obtained in each optimal topology presented, with a void placed in the center of the a repeating cell. The higher the nominal TCR, the larger the curvature of the arc-shaped boundary.

Based on observations of high-performing designs, a simpler computational model was pursued, namely one that assumed that the two sides of a conducting interface are always in contact, although possibly with zero normal pressure. Then, given fixed material properties, the effective thermal conductivity depends only on the contact pressure, which is in turn determined by the thermo-mechanical loading. A one-dimensional analytical solution verified the feasibility and desirability of this modeling simplification. A topology optimization approach based on a 2D finite element formulation was developed and used as a design tool for rectangular C3M cells. A novel iterative method was developed to address the inherent nonlinearity of the problem. An objective function with a direct relationship to the design goals was defined to ensure that the average temperature of the top surface of the cell did not exceed the hot limit for high heat loads or drop below the cold limit for low heat loads. Several examples of one-material and two-material designs with good performance under realistic heat loads were generated.

The bi-material T-shaped thermal switch design was reproduced in experimental prototypes. The thermal properties of the design were also validated with comparable TCC achieved; one sample having the lowest surface roughness of any tested yielded particularly promising performance. Moreover, the switching times assessed via electrical resistance across the gap, a limitation in DTE thermal switches, were small, in the vicinity of 60 s. The contact pressures evaluated using a theoretical TCC model were also consistent, based on comparison of experimental and theoretical TCC.

The use of the LM-RIF fabrication process was largely invalidated by the current work, with its major limitation the need to use nanometer-scale particles. The use of composite materials should be examined, as they create the possibility that other additive manufacturing approaches can be used to fabricate more sophisticated thermal switches. In preliminary 3D printing, a two color PLA was used to produce a geometrically-complex two-material design. Future 3-D additive fabrication methods could conceivably produce the elegant but complex material and geometric designs contemplated.

This investigation into C3M passive thermal control structures improved understanding of the problems involved in passive thermal control for spacecraft, and yielded new design procedures and optimization methods. Continued research is required to improve the robustness of the optimization scheme, as well as to experimentally verify the thermal performance of the resulting designs in practice.

References

Andreassen, E., Clausen, A., Schevenels, M., Lazarov, B. S., and Sigmund, O., "Efficient topology optimization in MATLAB using 88 lines of code," *Structural and Multidisciplinary Optimization*, Vol. 43, No. 1, Jan. 2011.

Antolino, N. E., et al. (2008). "Lost mold rapid infiltration forming of mesoscale ceramics: Part 1, fabrication." J. Am. Ceram. Soc. 92 (1, Suppl.): S63-S69.

Antolino, N. E., et al. (2008). "Lost mold-rapid infiltration forming of mesoscale ceramics: part 2, geometry and strength improvements." J. Am. Ceram. Soc. 92 (1, Suppl.): S70-S78.

Antonetti, V.W., T.D. Whittle and R.E. Simons, "An Approximate Thermal Contact Conductance," *Journal of Electronic Packaging Technical Briefs*, vol. 115, pp. 131-134, 1993.

Babcox, B. (2015). Processing of Nanoparticles for Thermal Switches, Unpublished communication.

Bharti, S., Frecker, M., Lesieutre, G., and Browne, J., "Tendon actuated cellular mechanisms for morphing aircraft wing," *SPIE Smart Structures and Materials*, 2007, San Diego, CA.

Bharti, S., M. Frecker, and G. Lesieutre. "A Methodology for Optimal Structural Design of a Morphing Aircraft Wing using Non-Dominated Sorting Genetic Algorithm II," *SPIE 13th International Symposium on Smart Structures and Materials*, 2006, San Diego, CA.

Facchinei, F., Jiang, H., and Qi, L., "A smoothing method for mathematical programs with equilibrium constraints," *Mathematical Programming*, Vol. 85, No. 1, May 1999, pp. 107-134.

Hayes, G. R., M. I. F., J. H. Adair (2011). "Fabrication of compliant mechanisms on the mesoscale." Mechanical Sciences 2: 129-137.

Hengeveld, D. W., M. M. M., James E. Braun, Eckhard A. Groll, Andrew D. Williams (2010). "Review of Modern Spacecraft Thermal Control Technologies." HAAC&R Research 16(2): 189-220.

Lesieutre, G.A., Browne, J.A., and Frecker, M., "Scaling and Performance, Weight, and Actuation of a 2-D Compliant Cellular Frame Structure for a Morphing Wing," *17th International Conference on Adaptive Structures and Technologies*, 2006, Taipei, Taiwan.

Marland, B., Bugdy, D., and Stouffer, C., "Development and testing of advanced cryogenic thermal switch concepts," *Space Technology and Applications International Forum*, Albuquerque, 2000.

Mehta, V., Frecker, M., and Lesieutre, G., "Contact-Aided Compliant Mechanisms for Morphing Aircraft Skin," *SPIE Smart Materials and Structures*, 2008, San Diego, CA.

Milanez, F. H., and Mantelli, M. B., "Theoretical and experimental studies of a bi-metallic heat switch for space applications," *International Journal of Heat and Mass Transfer*, vol. 46, no. 24, p. 4573–4586, 2003.

Novak, K. S., Phillips, C. J., Birur, G. C., Sunada E. T., and Pauken, M. T., "Development of a Thermal Control Architecture for the Mars Exploration Rovers," *Space Technology and Applications International Forum*, Albuquerque, 2003.

Paulsen, B. R., Batty, J. C., and Agren, J., "Cryogenic thermal diodes," *Space Technology and Applications International Forum - 2000*, Albuquerque, 2000.

Poole, W.J., M. F. A., N.A. Fleck (1996). "Micro-Hardness of Annealed and Work-Hardened Copper Polycrystals." Scripta Materialia 34(4): 559-564.

Ramrakhyani, D., G. Lesieutre, S. Bharti, and M. Frecker, "Aircraft Structural Morphing using Tendon Actuated Compliant Cellular Trusses," *Journal of Aircraft*, 2005. 42(6): p. 1615-1621.

Ramrakhyani, D., M. Frecker, G. Lesieutre, and S. Bharti. "Parallel Genetic Algorithm for Design of Morphing Cellular Truss Structures," *ASME International Mechanical Engineering Congress and Exposition*. 2005. Orlando, FL.

Sigmund, O., "Design of multiphysics actuators using topology optimization Part I: One-material structures," *Computer Methods in Applied Mechanics and Engineering*, vol. 190, no. 49, pp. 6577-6604, October 2001.

Sigmund, O., "Design of multiphysics actuators using topology optimization Part II: Two-material structures," *Computer Methods in Applied Mechanics and Engineering*, vol. 190, no. 49, pp. 6605-6627, October 2001.

Stavely, Rebecca L., "Design of Contact-Aided Compliant Cellular Mechanisms for Use as Passive Variable Thermal Conductivity Structures," M.S. thesis in Aerospace Engineering, The Pennsylvania State University, 2013.

Strömberg, N., Klarbring, A., "Topology optimization of structures in unilateral contact," *Structural and Multidisciplinary Optimization*, Vol. 41, No. 1, Feb 2010, pp. 57 - 64.

Sunada, E., Lankford, K., Pauken, M., Novak, K. S., and Birur, G., "Wax-actuated heat switch for Mars surface applications," *Space Technology and Applications International Forum* - 2002, Albuquerque, 2002.

Svanberg, K., "Method of Moving Asymptotes - a New Method for Structural Optimization," *International Journal for Numerical Methods in Engineering*, vol. 24, no. 2, pp. 359-373, February 1987

Thompson, B. C., Lloyd, B., Schick, S. H., and Li, L., "Cryogenic quad-redundant thermal switch," *Joint Cryogenic Engineering Conference/International Cryogenic Materials Conference*, Chattanooga, TN, 2007.

Thurier, P. F., "A Two-material Topology Optimization Method for the Design of a Passive Thermal Control Interface," M.S. thesis in Aerospace Engineering, The Pennsylvania State University, 2014.

Publications

1. Stavely, R.L., G.A. Lesieutre, M. Frecker, and J.H. Adair, "Variable Thermal Conductivity, Contact-Aided Cellular Structures For Spacecraft Thermal Control," *23rd International Conference on Adaptive Structures and Technologies (ICAST)*, October 11-13, 2012.
2. Stavely, R.L., Lesieutre, G.A., Frecker, M., Adair, J.H., "Variable Thermal Conductivity, Contact-Aided Cellular Structures for Spacecraft Thermal Control," paper AIAA 2013-1588, *proceedings of 54th AIAA/ASME/ASCE/AHS/ASC Structures, Structural Dynamics and Materials Conference*, April 8-11, 2013, Boston, MA.
3. Stavely, Rebecca L., "Design of Contact-Aided Compliant Cellular Mechanisms for Use as Passive Variable Thermal Conductivity Structures," M.S. thesis in Aerospace Engineering, The Pennsylvania State University, 2013.
4. Stavely, R.L., Lesieutre, G.A., Frecker, M., Adair, J.H., "Variable Thermal Conductivity, Contact-Aided Cellular Structures for Spacecraft Thermal Control," to be submitted to *Journal of Spacecraft and Rockets*, 2014.
5. Babcox, B.B., Lesieutre, G.A., Frecker, M.I., and Adair, J.H., "Theta Specimen Fabrication: From a Colloid to a Free-Standing Component," at the 88th ACS Colloid and Surface Science, Philadelphia, June 25-28, 2014.
6. Thurier, P.F., Lesieutre, G.A., Frecker, M.I., and Adair, J.H., "Design of Cellular Compliant Cell Mechanism for Thermal Control using Topology Optimization," *56th AIAA/ ASME/ ASCE/ AHS/ ASC Structures, Structural Dynamics, and Materials Conference*, AIAA SciTech 2015, Kissimmee, FL, January 5-9, 2015.
7. Thurier, P.F., Lesieutre, G.A., Frecker, M.I., and Adair, J.H., "Two-Material Topology Optimization for the Design of Passive Thermal Control Structures," *25th International Conference on Adaptive Structures and Technologies (ICAST)*, The Hague, The Netherlands, October 6-8, 2014.

8. Thurier, P. F., "A Two-material Topology Optimization Method for the Design of a Passive Thermal Control Interface," M.S. thesis in Aerospace Engineering, The Pennsylvania State University, 2014.
9. Thurier, P.F., Lesieutre, G.A., Frecker, M.I., and Adair, J.H., "Two-Material Topology Optimization for the Design of Passive Thermal Control Structures," submitted to *Journal of Intelligent Materials Systems and Structures,* 2015.
10. Thurier, P.F., Lesieutre, G.A., Frecker, M.I., and Adair, J.H., "Design of Cellular Compliant Cell Mechanism for Thermal Control using Topology Optimization," to be submitted to *Journal of Mechanical Design,* 2016.
11. Yu, T., "Topology Optimization Strategies for Multiphysics Problems," Ph.D. dissertation in Aerospace Engineering, The Pennsylvania State University, 2017 (expected).

Appendix: 3-D Printing of Thermal Switches

In recent years, technological and design advancements have led to the need for new fabrication methods that can produce parts in a rapid manner while not sacrificing resolution or cost effectiveness. The models designed in this report require such a fabrication technique (Figure 1).

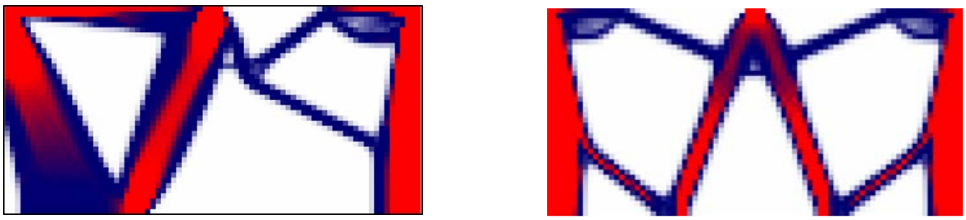

Figure 1. Multi-material optimized heat switches

To reproduce the multi-material designs with relatively small feature sizes rapid prototyping technology, specifically 3D printing, was implemented. Initially, models were fabricated using a Sonoplot GIX Microplotter II (Figure 2). However, this machine was limited due to its innate design for printing simple, single layer patterns of solutions containing conductive material or cells via a fragile, glass pipette.

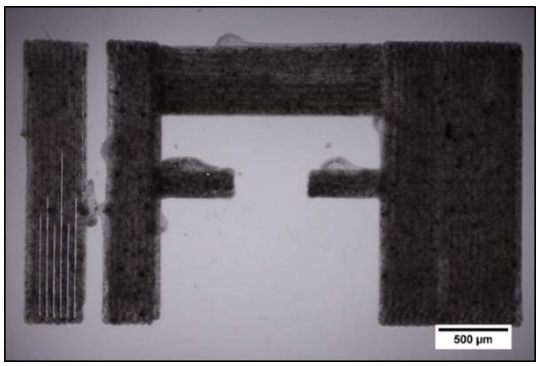

Figure 2. T-shaped cell printed with synthesized nanoscale copper paste

Nanoscale copper particles were synthesized at 14 weight percent and passivated by polyvinylpyrrolidone in a 70:30 Ethanol:water solution which provided a stable copper paste for over 8 months. To simplify the fabrication process future iterations will use a commercially available copper ink (Dupont CB200) printed with a retrofitted MakerGear M2 3D printer to allow for paste extrusion from a Structur3D Discov3ry (Figure 3).

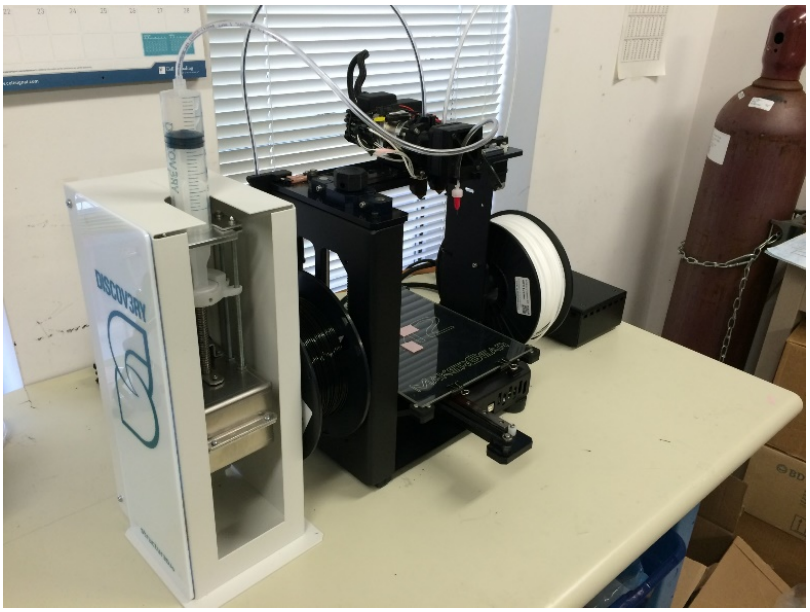

Figure 3. 3D printer setup with paste extruder modification

Resolution tests were designed to maximize spatial resolution for 3D printing of polymeric filament and paste extrusion by varying print speeds (Figure 4). The long term objective for optimizing printing capabilities is to be able to successfully fabricate the complex features shown in Figure 1 with a dual head paste extruder for high and low thermal conductivity inks.

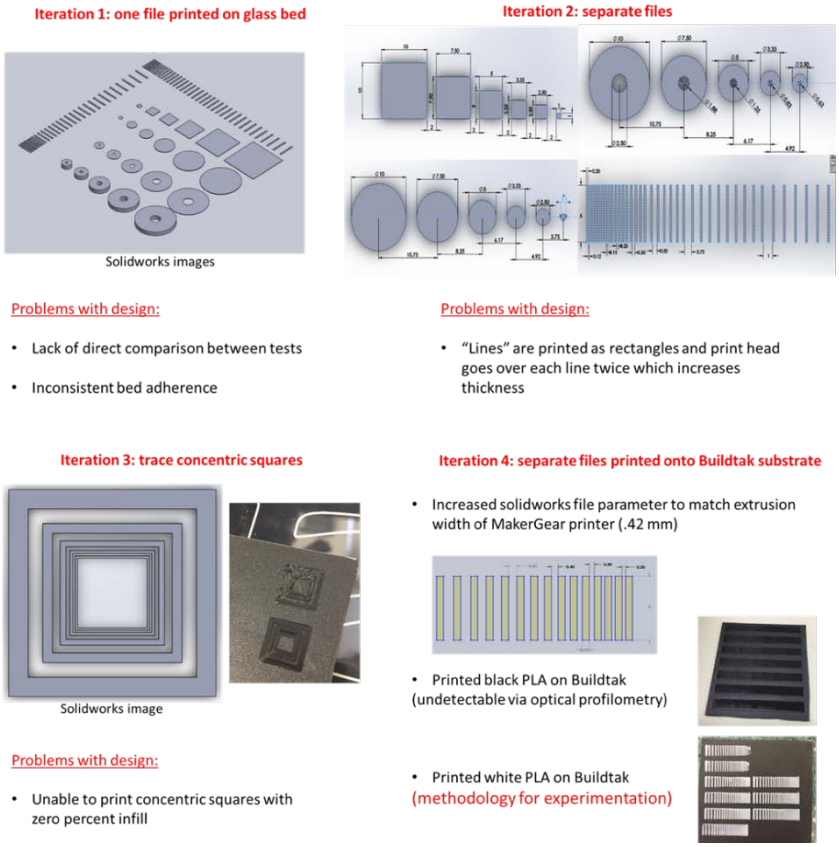

Figure 4. Resolution test development

Resolution in the X and Y direction in addition to simple shape accuracy were compared as a function of print speed. Using the design outlined in iteration 4, X and Y resolution were analyzed by printing the pattern shown in Figure 5.b at varying speeds. Figure 5.a depicts the print head path and print settings for each set of 10 traces with 9 troughs (3 at .3 mm, 3 at .2 mm, and 3 at .1 mm). The experiment was designed with the goal of being able to differentiate one .42 mm trace from another at a given separation distance (trough width). Figure 5.c shows optical profilometry data collected to quantitatively analyze surface roughness in addition to visualizing separation distance and overall print quality. CAD files were rotated for y spatial resolution testing with all other parameters remaining constant.

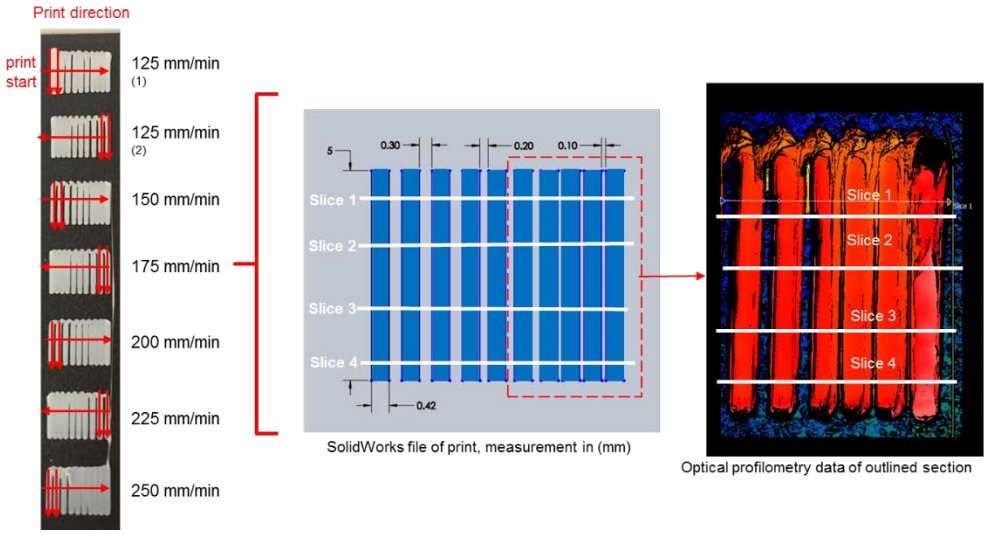

Figure 5. a) Print head and print settings. b) CAD model for x and y spatial resolution c) Optical profilometry scan example for x resolution

Data was collected and compared to expected values for trace height (.1 mm), trace width (.42 mm), trough width (.3, .2, or .1 mm), and trace length (5 mm) for both x and y resolution (Table 1 and Table 2 respectively). Expected values defined by CAD file.

Table 1: X resolution Data

Test	Speed (mm/min)	Measured Height (mm)	Expected Height (mm)	Measured Print Width (mm)	Expected Print Width (mm)	Measured Gap Width (mm)	Expected Gap Width (mm)	Measured Length (mm)	Expected Length (mm)	Average Percent Error
RWM1-8B1	**100**	0.1350	0.10	0.5621	0.42	0.1640	0.30	4.300	5	**32.04%**
RMW1-8A3(1)	**100**	0.1620	0.10	0.3990	0.42	0.4270	0.40	3.915	5	**23.86%**
RWM1-8A5(2)	**200**	0.1381	0.10	0.4410	0.42	0.2356	0.20	4.288	5	**16.29%**
RWM1-8B3(1)	**250**	0.1539	0.10	0.4694	0.42	0.229	0.30	3.837	5	**28.15%**
RWM1-8B3(2)	**250**	0.1308	0.10	0.5734	0.42	0.2323	0.40	4.111	5	**32.86%**
RWM1-8B4(1)	**300**	0.1591	0.10	0.6120	0.42	0.2129	0.40	4.212	5	**41.84%**
RWM1-8B4(2)	**300**	0.1199	0.10	0.6841	0.42	0.1527	0.40	4.604	5	**38.13%**
RWM1-8B5(2)	**350**	0.0965	0.10	0.7550	0.42	0.1593	0.50	4.679	5	**39.46%**
RWM1-8B6(1)	**400**	0.1125	0.10	0.7408	0.42	0.1625	0.50	4.951	5	**39.34%**

Table 2: Y resolution Data

Test	Speed (mm/min)	Measured Height (mm)	Expected Height (mm)	Measured Print Width (mm)	Expected Print Width (mm)	Measured Gap Width (mm)	Expected Gap Width (mm)	Measured Length (mm)	Expected Length (mm)	Average Percent Error
RMW1-8 1(1)	**100**	0.2403	0.10	0.5524	0.42	0.3217	0.30	3.435	5	**48.97%**
RMW1-8 1(2)	**100**	0.1840	0.10	0.4090	0.42	0.1983	0.20	4.082	5	**26.46%**
RMW1-8 2(1)	**150**	0.1410	0.10	0.4564	0.42	0.2826	0.30	4.208	5	**17.56%**
RMW1-8 3(1)	**200**	0.1470	0.10	0.4907	0.42	0.2404	0.30	4.288	5	**21.53%**
RMW1-8 4(1)	**250**	0.122	0.10	0.6387	0.42	0.1600	0.40	4.625	5	**35.39%**
RMW1-8 5(1)	**300**	0.078	0.10	0.958	0.42	0.2070	0.60	4.772	5	**63.49%**

An average percent error was calculated by taking the mean of percent errors for the four measurements. The average percent area was then plotted against print speed to determine the minimum, ideal printing speed for both x and y spatial resolution (200 and 150 mm/min respectively) (Figure 6).

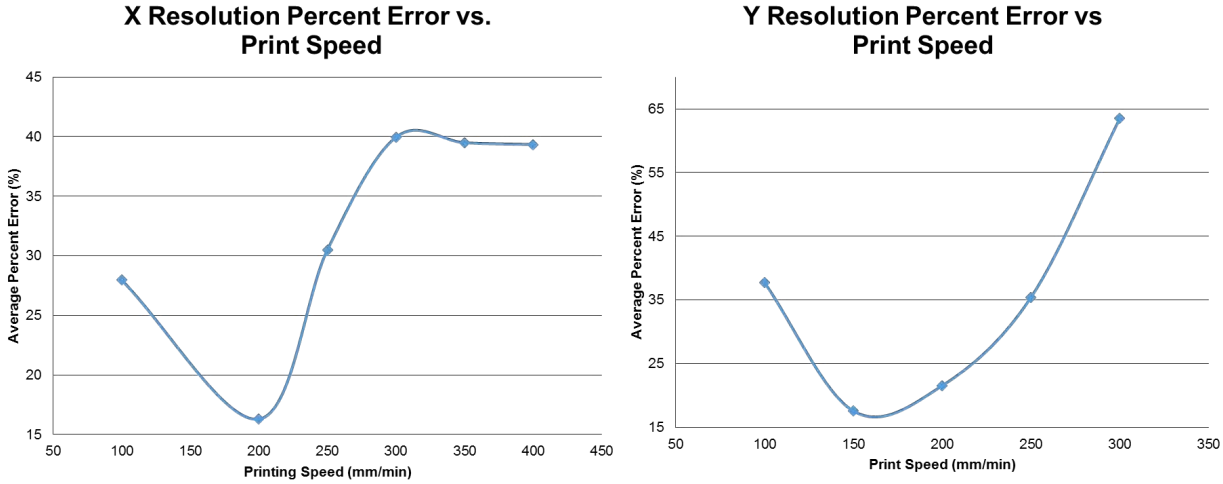

Figure 6. X and Y spatial resolution for minimized average percent error

This parameter was averaged to a print speed of 175 mm/min for all future tests and printed parts. Preliminary work on determining the effect of print speed on shape accuracy has begun, but requires additional work for statistical analysis (Figure 7). In addition, future studies conducted will analyze the effects of nozzle diameter, print bed temperature, extruder temperature, and different materials (polymeric filaments and pastes) on spatial resolution and shape accuracy.

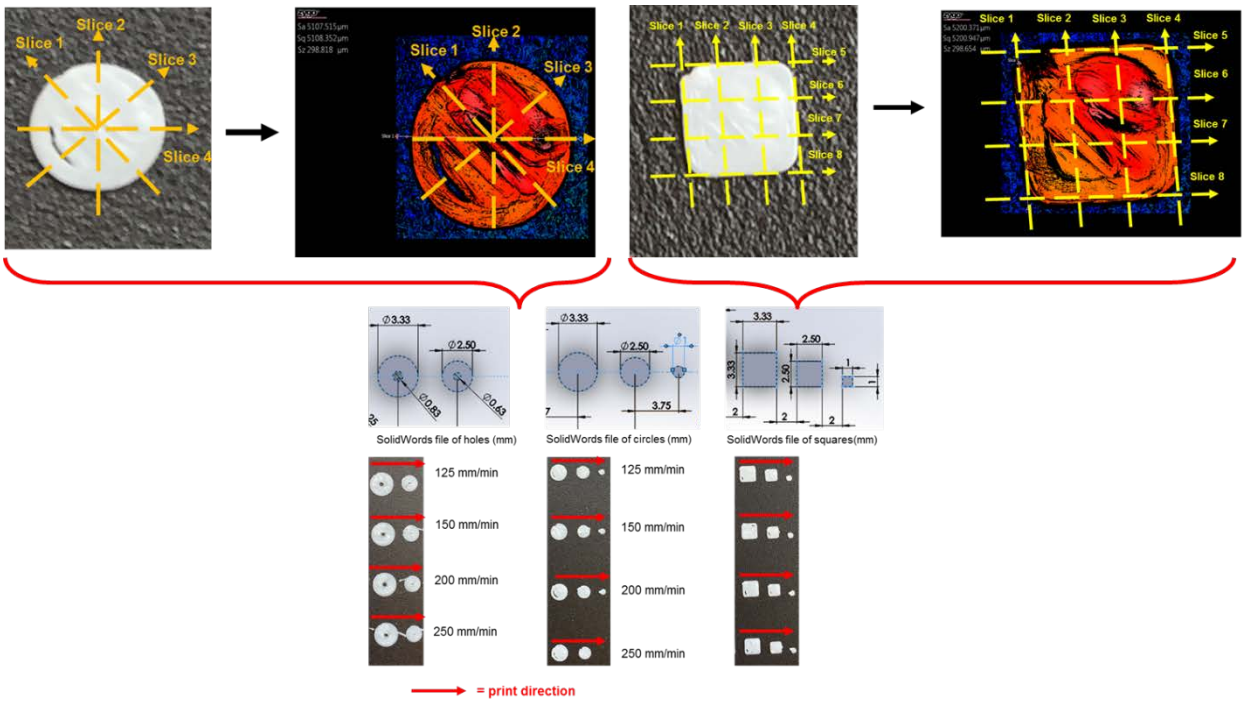

Figure 7. Preliminary data collection setup for shape resolution experimentation

From the information gained through the optimization process for 3D printing, attempts have been made to print multi-material polymeric heat switches following the design in Figure 1, in addition to copper paste extrusion printed T-shape cells (Figure 8). Further testing is needed to continue the optimization process and move towards a multi-material paste extrusion system that can use a copper and zirconia paste to accurately represent the functionality of the heat switches.

Figure 8. 3D printed parts of optimized designs

AFOSR Deliverables Submission Survey

Response ID:7185 Data

1.

Report Type

Final Report

Primary Contact Email

Contact email if there is a problem with the report.

g-lesieutre@psu.edu

Primary Contact Phone Number

Contact phone number if there is a problem with the report

814-863-0103

Organization / Institution name

The Pennsylvania State University

Grant/Contract Title

The full title of the funded effort.

MULTIFUNCTIONAL THERMAL STRUCTURES USING CELLULAR CONTACT-AIDED COMPLIANT MECHANISMS

Grant/Contract Number

AFOSR assigned control number. It must begin with "FA9550" or "F49620" or "FA2386".

FA9550-11-1-0232

Principal Investigator Name

The full name of the principal investigator on the grant or contract.

George A. Lesieutre

Program Officer

The AFOSR Program Officer currently assigned to the award

Dr. Byung-Lip Lee

Reporting Period Start Date

08/01/2011

Reporting Period End Date

07/31/2016

Abstract

Thermal management of spacecraft electronics is a major concern. Passive thermal control promises high reliability and reduced system weight. Cellular contact-aided compliant mechanisms were considered as an avenue to variable thermal conductivity. Thermally-driven deformation creates or breaks contact or modifies contact pressure, thereby controlling heat conduction through an interface. Pressure-dependent thermal contact conductance generates a smooth change between insulating and conducting modes. A topology optimization approach was conceived to maximize performance by placing two materials having very different conductivities. Several designs with good performance under realistic high and low heat loads were generated. Bi-material prototypes were fabricated from polished copper sheet. They achieved good conductance and rapid switching, especially those having low surface roughness. Future 3-D additive fabrication methods could conceivably produce the elegant but complex material and geometric designs contemplated. Continued research is needed to improve the robustness of the optimization scheme, as well as to fabricate and experimentally verify the thermal performance of the resulting designs in practice.

Distribution Statement

This is block 12 on the SF298 form.

Distribution A - Approved for Public Release

Explanation for Distribution Statement

If this is not approved for public release, please provide a short explanation. E.g., contains proprietary information.

SF298 Form

Please attach your SF298 form. A blank SF298 can be found here. Please do not password protect or secure the PDF The maximum file size for an SF298 is 50MB.

SF298_FA9550-11-1-0232.pdf

Upload the Report Document. File must be a PDF. Please do not password protect or secure the PDF . The maximum file size for the Report Document is 50MB.

FinalReport_FA9550-11-1-0232.pdf

Upload a Report Document, if any. The maximum file size for the Report Document is 50MB.

Archival Publications (published) during reporting period:

1. Stavely, R.L., G.A. Lesieutre, M. Frecker, and J.H. Adair, "Variable Thermal Conductivity, Contact-Aided Cellular Structures For Spacecraft Thermal Control," 23rd International Conference on Adaptive Structures and Technologies (ICAST), October 11-13, 2012.
2. Stavely, R.L., Lesieutre, G.A., Frecker, M., Adair, J.H., "Variable Thermal Conductivity, Contact-Aided Cellular Structures for Spacecraft Thermal Control," paper AIAA 2013-1588, proceedings of 54th AIAA/ASME/ASCE/AHS/ASC Structures, Structural Dynamics and Materials Conference, April 8-11, 2013, Boston, MA.
3. Stavely, Rebecca L., "Design of Contact-Aided Compliant Cellular Mechanisms for Use as Passive Variable Thermal Conductivity Structures," M.S. thesis in Aerospace Engineering, The Pennsylvania State University, 2013.
4. Stavely, R.L., Lesieutre, G.A., Frecker, M., Adair, J.H., "Variable Thermal Conductivity, Contact-Aided Cellular Structures for Spacecraft Thermal Control," to be submitted to Journal of Spacecraft and Rockets, 2014.
5. Babcox, B.B., Lesieutre, G.A., Frecker, M.I., and Adair, J.H., "Theta Specimen Fabrication: From a Colloid to a Free-Standing Component," at the 88th ACS Colloid and Surface Science, Philadelphia, June 25-28, 2014.
6. Thurier, P.F., Lesieutre, G.A., Frecker, M.I., and Adair, J.H., "Design of Cellular Compliant Cell Mechanism for Thermal Control using Topology Optimization," 56th AIAA/ ASME/ ASCE/ AHS/ ASC Structures, Structural Dynamics, and Materials Conference, AIAA SciTech 2015, Kissimmee, FL, January 5-9, 2015.
7. Thurier, P.F., Lesieutre, G.A., Frecker, M.I., and Adair, J.H., "Two-Material Topology Optimization for the Design of Passive Thermal Control Structures," 25th International Conference on Adaptive Structures and Technologies (ICAST), The Hague, The Netherlands, October 6-8, 2014.
8. Thurier, P. F., "A Two-material Topology Optimization Method for the Design of a Passive Thermal Control Interface," M.S. thesis in Aerospace Engineering, The Pennsylvania State University, 2014.
9. Thurier, P.F., Lesieutre, G.A., Frecker, M.I., and Adair, J.H., "Two-Material Topology Optimization for the Design of Passive Thermal Control Structures," submitted to Journal of Intelligent Materials Systems and Structures, 2015.
10. Thurier, P.F., Lesieutre, G.A., Frecker, M.I., and Adair, J.H., "Design of Cellular Compliant Cell Mechanism for Thermal Control using Topology Optimization," to be submitted to Journal of Mechanical Design, 2016.
11. Yu, T., "Topology Optimization Strategies for Multiphysics Problems," Ph.D. dissertation in Aerospace Engineering, The Pennsylvania State University, 2017 (expected).

New discoveries, inventions, or patent disclosures:

Do you have any discoveries, inventions, or patent disclosures to report for this period?

No

Please describe and include any notable dates

Do you plan to pursue a claim for personal or organizational intellectual property?

Changes in research objectives (if any):

None

Change in AFOSR Program Officer, if any:

None

Extensions granted or milestones slipped, if any:

None

AFOSR LRIR Number

LRIR Title

Reporting Period

Laboratory Task Manager

Program Officer

Research Objectives

Technical Summary

Funding Summary by Cost Category (by FY, $K)

	Starting FY	FY+1	FY+2
Salary			
Equipment/Facilities			
Supplies			
Total			

Report Document

Report Document - Text Analysis

Report Document - Text Analysis

Appendix Documents

2. Thank You

E-mail user

Oct 30, 2016 19:59:14 Success: Email Sent to: g-lesieutre@psu.edu